Diplomarbeit

Measurement of the relative $\chi_{b2}(1P)/\chi_{b1}(1P)$ polarization in proton-proton collisions at $\sqrt{s} = 13\,\mathrm{TeV}$

ausgeführt am

Atominstitut der Fakultät für Physik der Technischen Universität Wien
in Zusammenarbeit mit dem Institut für Hochenergiephysik (HEPHY)
der Österreichischen Akademie der Wissenschaften (ÖAW)

unter der Anleitung von

Univ.Doz. Dipl.-Ing. Dr.techn. Claudia-Elisabeth Wulz

eingereicht von

Jakob Necker
Matrikelnummer 00925662

Eingereicht zur Erlangung des akademischen Grades Diplom-Ingenieur
im Rahmen des Masterstudiums Technische Physik

Wien, im September 2018 _____

Contents

Chapter 1

Introduction

The χ_b meson is a bound state of a bottom quark and its antiquark and hence belongs to the family of quarkonia, which designate the bound states of heavy quarks and their respective antiquarks. Generically these are referred to as bottomonium ($b\bar{b}$) and charmonium ($c\bar{c}$). More than four decades after the discovery of the first quarkonium sate, the J/ψ meson, quarkonium physics is still an active field of fundamental research since it serves as an excellent laboratory for testing the standard model (SM) of particle physics. Measurements of the polarization of bottomonium, especially of the P-wave states, which are investigated in this work, are important to verify predictions of quantum chromodynamics (QCD). Until now, only the polarization of S-wave bottomonium states has been measured.

The Large Hadron Collider (LHC), located near Geneva, Switzerland, provides an ideal source of quarkonia. The Compact Muon Solenoid (CMS) detector, which is placed at one of the four collision points of the LHC records the particles emerging from the high-energy proton-proton (pp) collisions. This thesis deals with a first polarization analysis of the $\chi_b(1P)$ states using data taken at CMS in the years 2016 and 2017 at a center-of-mass energy of $\sqrt{s} = 13\,\text{TeV}$. It has to be noted that in this work natural units are used, therefore $\hbar = c = 1$, where c is the speed of light and $\hbar$ the reduced Planck constant.

At first an introduction of the LHC and the European Organization for Nuclear Research (CERN) is given in Chapter 2, followed by an introduction of the CMS detector and its different subdetector systems in Chapter 3.

At the beginning of Chapter 4, in Section 4.1, the standard model of particle physics and QCD, the theory describing the strong interaction, are briefly discussed. Then, in Section 4.2 quarkonium spectra are introduced, and in Section 4.3 the basic ideas of the most important theoretical descriptions of the production of quarkonium are presented. The theory concerning the polarization of quarkonium is discussed in Section 4.4. In Section 4.5 the current situation of bottomonium measurements is summarized and some

recent results are shown.

In Chapter 5 the analysis of the relative $\chi_{b2}(1P)/\chi_{b1}(1P)$ polarization is reported. The chapter starts with a summary of the analysis strategy in Section 5.1. Details on the used data samples are given in Section 5.2. For the extraction of the relative $\chi_{b2}(1P)/\chi_{b1}(1P)$ event yields two different methods are used, which are discussed in Sections 5.3 and 5.4, followed by the estimation of systematic uncertainties in Section 5.5. The obtained $\chi_{b2}(1P)/\chi_{b1}(1P)$ event yields are then presented in Section 5.6.

In Chapter 6 the obtained relative $\chi_{b2}(1P)/\chi_{b1}(1P)$ polarization is compared to samples with different polarization scenarios produced in a simulation.

The author contributed to the measurement of the χ_{bJ} polarization (J denotes the total angular momentum) by making a first measurement of the relative polarization of $\chi_{b2}(1P)$ to $\chi_{b1}(1P)$ mesons, including the prior processing of the data which was taken at the CMS detector in the years 2016 and 2017. For this thesis two different methods for obtaining the relative polarization have been investigated. It became apparent that for both methods a larger data sample is required to attain significant results.

Chapter 2

CERN and the LHC

The European Organization for Nuclear Research (CERN) has its origins in the early 1950s, when a group of European scientists, among them Niels Bohr and Pierre Auger, had the vision of a European nuclear physics laboratory. In 1952 an agreement that established a provisional council was signed by 11 countries. The council decided to build the CERN laboratory near Geneva in Switzerland, and the first accelerator, the 600 MeV Synchrocyclotron, started up in 1957. Now CERN is the world's leading research facility in particle physics and can point to a lot of achievements over the past 60 years. Beyond the achievements in fundamental research, such as the discovery of the W [1, 2] and Z [3, 4] bosons in 1983 or the Higgs boson in 2012 [5, 6], technologies like the World Wide Web (WWW) [7] also have their origin at CERN [8].

During the last decades, a vast complex of accelerators was built at the CERN site. The accelerator complex is a chain of different machines which sequentially increases the energy of protons or lead ions, to collide them finally in one of the four interaction points (IPs) of the Large Hadron Collider (LHC). The LHC is located approximately 100 m underground in a tunnel of 27 km circumference. It has two beam pipes in which the charged particles, most of the time protons, circulate in opposite directions to finally collide at a center-of-mass energy $\sqrt{s} = 13\,\text{TeV}$. But before, the protons have to make a long journey through the whole acceleration chain [9].

Their journey starts in a bottle of hydrogen gas, from where the hydrogen atoms are injected in an electrical field to extract the protons by stripping off the electrons. After the protons have been isolated, a first push of the linear accelerator 2 (Linac2) provides them with an energy of 50 MeV. They are then forwarded to the Proton Synchrotron Booster (PSB), where they reach an energy of 1.4 GeV. After passing another two accelerators, the Proton Synchrotron (PS) and the Super Proton Synchrotron (SPS), the protons arrive at the LHC beam pipes with 450 GeV. The beam is now bundled in packets of 1.15×10^{11} protons, where one beam can currently

contain a maximum of 2556 such packets [10], which are called bunches. These bunches of protons are injected in opposite direction into the two beam pipes of the LHC and are then accelerated up to an energy of 6.5 GeV each. Finally, the two counter-circulating beams collide in the four IPs of the LHC. From the energy released by the collision a firework of particles emerges. A schematic diagram of the accelerators and the detectors situated at the CERN site is shown in Fig. 1.

Various experiments are situated throughout the whole chain of accelerators, the four biggest are located at the four IPs of the LHC, they are:

- A Large Ion Collider Experiment (ALICE),
- A Toroidal LHC Apparatus (ATLAS),
- Compact Muon Solenoid (CMS),
- LHC beauty (LHCb).

The ALICE detector is, as the name already indicates, particularly designed for the measurement of lead-ion collisions, to study the properties of the quark-gluon plasma. The purpose of ATLAS as well as of CMS is to cover the widest possible range of physics. Both of them try to reach this goal

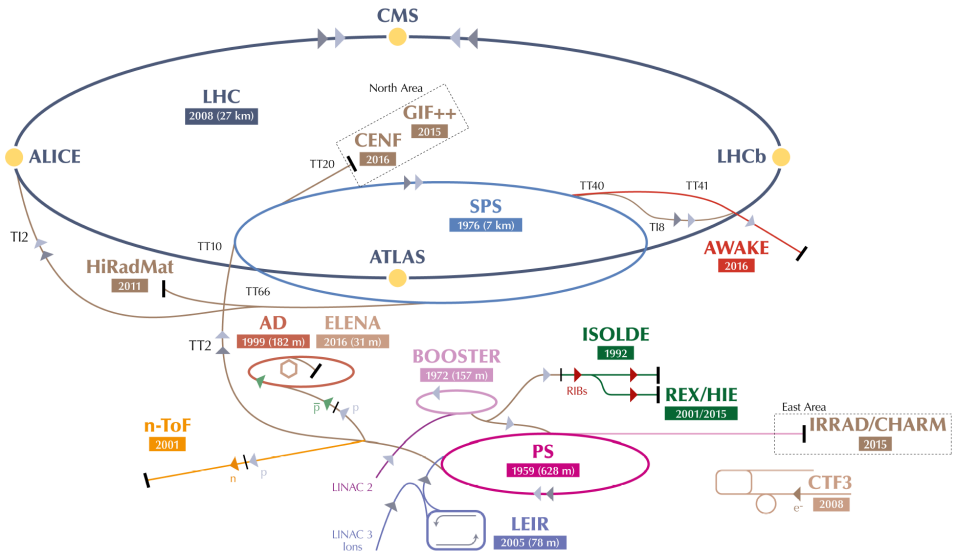

Figure 1: The LHC accelerator complex. The acceleration of the protons for the LHC starts at the Linac2, goes on to the PSB (labeled BOOSTER in the diagram), the PS, the SPS and finally reaches the LHC. The four IPs of the LHC, as well as the four biggest experiments located there, are marked with a yellow dot. The remaining accelerators and detectors are not discussed in this work. From Ref. [11].

with different approaches in the detector design. Especially the magnetic field of the two detectors differs: while ATLAS has a toroidal magnetic field, CMS uses a twice as strong solenoidal field of 3.8 T. In comparison to the compact solenoid of CMS, ATLAS has an enormous magnetic system, which consists of eight 25 m long superconducting magnet coils. The LHCb experiment is optimized for detecting B mesons. Since B mesons fly more likely in directions close to the line of the beam pipe, the detector is built as a 20 m long series of subdetectors which are positioned along the beam line. The main physics aim of LHCb is to study the asymmetry between matter and antimatter.

In the following chapter a more detailed discussion of the CMS detector, which supplies the data for this thesis, is given.

Chapter 3

The CMS detector

The CMS detector is a general-purpose detector having a broad physics program, which ranges from the detailed study of the standard model to the search for dark matter and supersymmetry (SUSY). To reach these goals the detector is required to have, among others [12]:

- Good muon identification and momentum resolution over a wide range.
- Good dimuon mass resolution of $\approx 1\%$ at 100 GeV.
- Good charged-particle momentum resolution and reconstruction efficiency in the inner tracker.
- Good electromagnetic energy resolution, good diphoton and dielectron mass resolution ($\approx 1\%$ at 100 GeV) and good π^0 rejection.

A detailed description of the CMS detector and its design can be found in Refs. [12], [13] and [14].

The dimensions of the detector are 21.6 m in length and 15 m in diameter with a total mass of 12 500 t. The essential part of the detector is a four tesla superconducting solenoid with a length of 13 m and an inner diameter of 6 m. The innermost layer of the detector, the inner tracking system, which is made entirely of silicon, as well as the Electromagnetic Calorimeter (ECAL) and the Hadron Calorimeter (HCAL) are located within the solenoid. The muon system is positioned outside of the magnet. A schematic drawing of the detector is shown in Fig. 2.

For the measurement of the position of the particles a coordinate system has to be defined. The origin of the coordinate system of the CMS detector is centered at the nominal collision point in the middle of the detector. The z axis points along the beam direction, the x axis points radially inward, toward the center of the LHC ring, and the y axis points vertically upwards. The azimuthal angle ϕ is measured from the x axis in the x-y plane and the polar angle θ from the z axis.

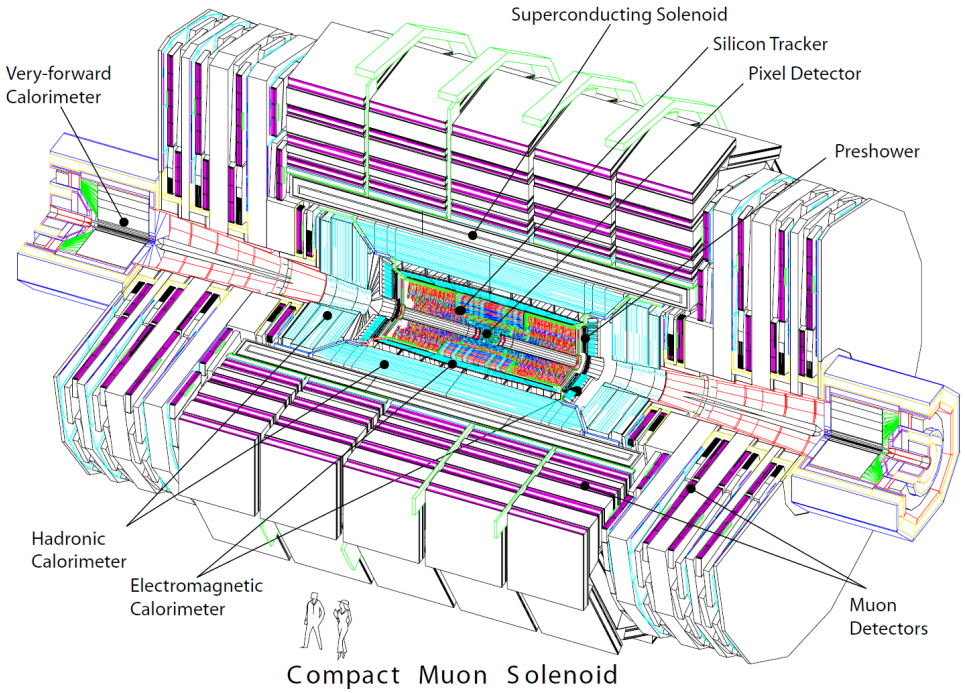

Figure 2: The detector system of the CMS. The proton beams enter the detector through the openings in the center of the left and the right side and are brought to collision right in the middle of the detector. From Ref. [15].

An important quantity that is related to the polar angle is the pseudorapidity η, which can be defined in two ways

$$\eta = -\ln\left(\tan(\theta/2)\right) = \frac{1}{2}\ln\left(\frac{p + p_{\mathrm{L}}}{p - p_{\mathrm{L}}}\right), \tag{3.1}$$

where p is the magnitude of the total momentum and p_{L} is the longitudinal component (the z component) of the momentum. The variable η is used to describe the angle of a particle relative to the beam axis. The region $|\eta| < 1.2$ is called barrel region, and the region of $0.9 < |\eta| < 2.5$ is denoted as endcap region within the CMS detector. Pseudorapidity is closely related to the rapidity y, which is defined in high energy physics as

$$y = \frac{1}{2}\ln\left(\frac{E + p_{\mathrm{L}}}{E - p_{\mathrm{L}}}\right), \tag{3.2}$$

where E is the total energy. From Eq. 3.1 it can be seen that if the mass of the particle is negligible compared to its momentum p (and hence $E \approx p$), the pseudorapidity converges to the rapidity, $\eta \approx y$. For massless particles, such as the photon, this means that $\eta \equiv y$.

The transverse momentum p_{T} and energy E_{T} denote the magnitude of the (x, y) component of the momentum and the energy, respectively.

The purpose of the detector system is to record characterizing information about all particles involved in an event, so that the whole process can be reconstructed and the particles can be identified and counted. The particular requirements on the detector design deduce from the need to detect high energetic standard model particles originating from rapidly decaying particles. Therefore the detector must be able to distinguish and measure the momenta of photons, electrons, muons and hadron jets. All these demands are fulfilled by the CMS detector by a sophisticated arrangement of different detector systems around a huge solenoid magnet. Figure 3 shows how the different particles are identified through the characteristic signature they leave in the detector:

- **Photons** and **electrons** are both stopped in the Electromagnetic Calorimeter. They can be distinguished through the track they leave (electrons) or do not leave (photons) in the silicon tracker.
- **Hadrons** are stopped in the Hadron Calorimeter. Charged hadrons are bent by the magnetic field and detected by the tracker as well as by the HCAL, neutral hadrons only interact with the HCAL.
- **Muons** are the only charged particles that traverse the whole detector and hence are detected by the muon system as well as by the inner tracker.

- The presence of **neutrinos**, which do not interact with any of the detector layers, is inferred from the missing transverse momentum vector, which is defined as the projection onto the plane perpendicular to the beam axis of the negative vector sum of the momenta of all reconstructed particle-flow objects in an event.

Before more details on the different parts of the CMS detector are provided in the next sections, it is necessary to introduce some terminology that is important for the further discussion. The term pileup denotes the phenomenon of multiple proton-proton (pp) collisions occurring during one bunch crossing. The overall information produced at one bunch crossing, including all pileup collisions is called event. To describe the performance of a particle accelerator an important quantity is the instantaneous luminosity L. The luminosity is defined as the conversion factor from a cross section σ to the number N of produced pp collisions [17]:

$$\frac{\mathrm{d}N}{\mathrm{d}\Omega} = L\frac{\mathrm{d}\sigma}{\mathrm{d}\Omega}, \tag{3.3}$$

where Ω is the solid angle for the angular differential cross section. For two colliding bunches with n_1 and n_2 particles, randomly distributed within the

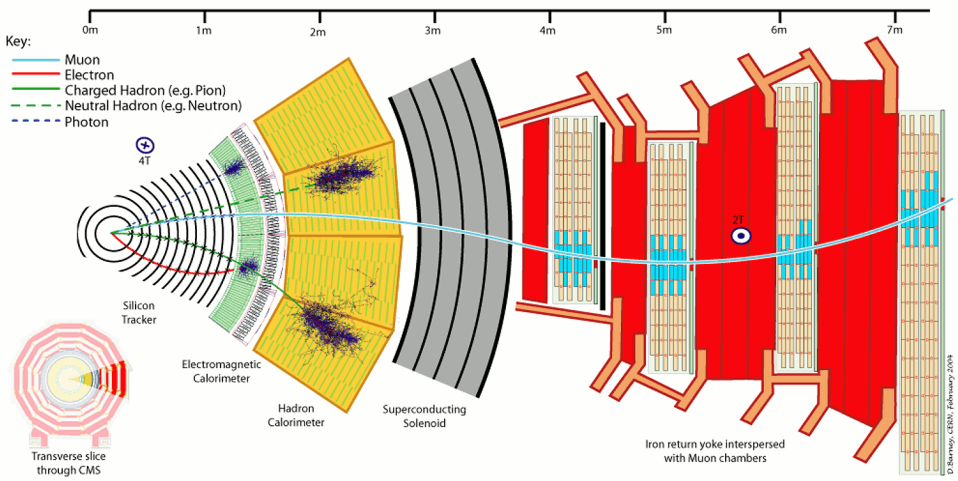

Figure 3: A twelfth of a transverse slice through the CMS detector. Only muons reach the outermost part of the detector, the muon chambers. Hadrons are stopped by the HCAL while photons and electrons are stopped by the ECAL. Charged particles, such as muons, electrons and charged hadrons, leave a track in the silicon tracker, whereas photons and neutral hadrons do not. The magnetic field is parallel to the beam axis, within the superconducting solenoid it points in the opposite direction than outside. From Ref. [16].

bunches, an impact area A and a repetition frequency ν_n one obtains:

$$L = \nu_n \cdot \frac{n_1 \cdot n_2}{A}. \tag{3.4}$$

Integrating the luminosity over time gives the integrated luminosity $\mathcal{L}$, which reflects the total collected amount of data and is usually given in units of inverse femtobarn (fb^{-1}), where 1 b equals $10^{-24}\,\mathrm{cm}^2$.

3.1 Inner tracking system

The purpose of the inner tracking system is the precise and efficient measurement of the tracks of charged particles to determine their momenta as well as to reconstruct the location of the vertex (the position of the particle interaction). Because of the almost homogeneous magnetic field, the momentum of the charged particles can be obtained directly from the curvature of the tracks, which is induced by the Lorentz force, which depends on the magnetic field and the particle's momentum and charge. At the LHC design luminosity of $10^{34}\,\mathrm{cm}^{-2}\,\mathrm{s}^{-1}$, about 1000 particles from more than 20 overlapping pp interactions are crossing the tracker system in each bunch collision. This requires fine granularity and fast response, but also a material that withstands such a severe radiation. All these requirements are fulfilled by the application of an entirely silicon-based system. The inner tracker consists of two parts, the pixel and the strip tracker. Between the data taking periods 2016 and 2017 the pixel detector was upgraded [18]. Since in this thesis data from both of these data taking periods are analyzed, it is important to be aware of the changed settings, which have an impact on the charged particle tracking efficiency as well as on the performance of electron and photon identification. Before the upgrade the pixel detector had three, and after the upgrade four cylindrical layers of pixel modules, which are positioned at 2.9 cm, 6.8 cm, 10.9 cm and 16 cm from the beam pipe, with an area of the sensor cells of $100\,\mu\mathrm{m}^2 \times 150\,\mu\mathrm{m}^2$. Cylindrically around the pixel detector ten layers of silicon strip detectors are placed, reaching a radius of 1.3 m.

3.2 Calorimeters

In contrast to the tracker, which should interact as little as necessary with the particles, the calorimeter measures the energy and direction of particles by fully absorbing them. There are two calorimeters, the Electromagnetic Calorimeter, for measuring the energy of electrons and photons, and the Hadron Calorimeter, to obtain the energy of hadrons, such as protons, neutrons, pions or kaons.

The ECAL is made of lead tungstate ($PbWO_4$) crystals, which are producing photons in an amount proportional to the particle energy. The scintillation light is detected by photodetectors that are mounted at the back of the crystals. The ECAL is composed of a barrel region with 61 200 high-density crystals and two endcaps with 7324 crystals each. To not be fooled by neutral pions (π^0), which can be misinterpreted as high-energy photons when they decay into two close low-energy photons, so called preshower detectors are placed in front of the ECAL endcaps.

The aim of the HCAL is to capture every particle that emerged from the collision (and has not been detected by the ECAL or is a muon or a neutrino) to be able to indirectly infer the presence of non-interacting uncharged particles, such as neutrinos. The HCAL consists of layers of brass and steel interleaved with tiles of plastic scintillators that are arranged without leaving any gaps through which a detectable particle might escape. This arrangement of repeating layers of dense absorber and plastic scintillator tiles allows the detection of the particle's position, energy and arrival time.

3.3 Superconducting solenoid

Obtaining a good momentum resolution, even for high-energetic particles, requires a strong magnetic field with a strong bending power. For the muon system a high magnetic field is particularly necessary to clearly determine the charge of the muon, especially for high p_T muons. The main strengths of a solenoidal magnetic field are that the field has spatial uniformity throughout the whole tracking volume and that high p_T particles travel perpendicular to the magnetic field, which allows a precise measurement of the momentum. The magnetic field of a solenoid can be calculated as $B = \mu_0 n I$, with n being the number of turns per meter, I the current and μ_0 the vacuum permeability. To achieve a momentum resolution of $\frac{\Delta p}{p} \approx 10\%$ at 1 TeV a magnetic field of 4 T is needed. Such a high field is reached with a high-purity aluminum-stabilized conductor, wrapped 2168 times at a length of 12.9 m and with a current of 19.5 kA. A return steel yoke, which is positioned between the single muon detector parts, closes the field lines.

3.4 Muon system

As muons are highly penetrating and can pass through the ECAL and HCAL, they are the only particles to reach the muon detectors. Therefore the muon detector is ideal for identifying and hence triggering on muons. The CMS muon system is capable of reconstructing the momentum and charge of muons over the entire kinematic range of the LHC. The system, which is integrated in the return yoke structures of the magnetic system,

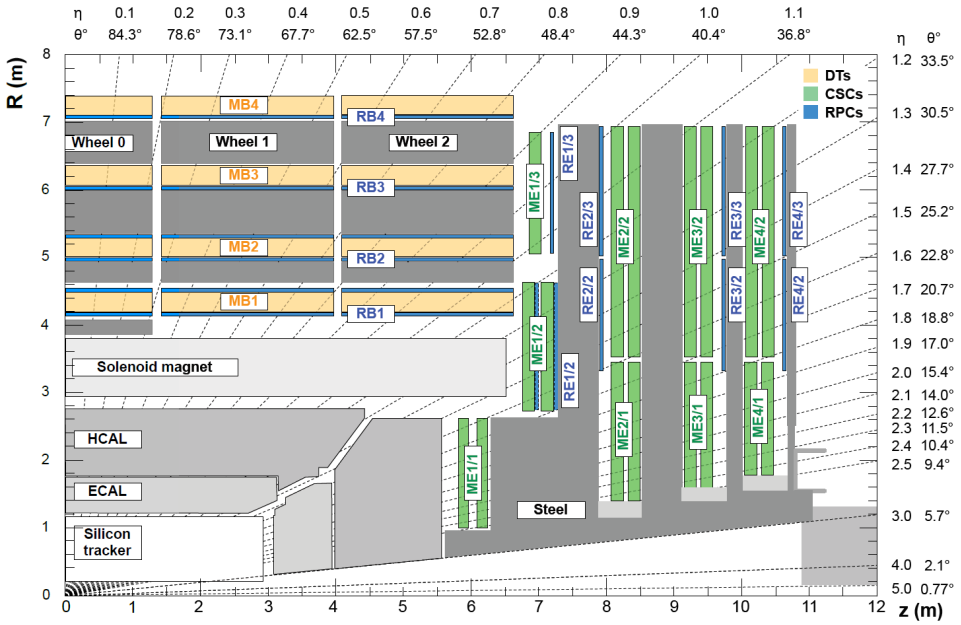

Figure 4: Layout of one quarter of the CMS muon system with the RPCs (blue), the DTs (orange) and the CSCs (green). The IP is in the lower left corner. From Ref. [19]

consists of Resistive Plate Chambers (RPCs), Drift Tubes (DTs) and Cathode Strip Chambers (CSCs), which are arranged as shown in Fig. 4.

The DT chambers consist of 4 stations and are positioned in the outermost barrel region of the detector, where the neutron induced background is small and the muon rate is low. They are filled with a mixture of argon (85%) and CO_2 (15%) gas molecules, which are ionized when a muon enters the chamber. The resulting ions and electrons end up at a charged wire where they produce an electric current. Together with the information of the drift time between impact and signal the y and z coordinates are obtained.

The CSCs are positioned in the endcap region, where the magnetic field is uneven and the neutron induced background rate is high. Positively-charged anode wires are crossed with negatively-charged cathode strips to build an array that allows not only very fast triggering thanks to the anode wire, but also a precise determination of the coordinates of the muons with help of the cathode strip. The resolution of the two position coordinates is about 200 µm.

The RPCs are positioned at the crossover of barrel and endcap region. They provide a fast response with a time resolution of just one nanosecond but a coarser position resolution than the CSCs and DTs.

3.5 Trigger system

The LHC was designed for a bunch crossing rate of 40 MHz, which corresponds to an interaction every 25 ns. When considering a pileup of 25, CMS has to deal with a billion pp collisions every second. Since every event produces about 1 MB of data, every second around 40 TB of data are generated, which can, with today's technologies, not all be stored permanently. Therefore it has to be decided which events are worth keeping and which should be rejected. This selection of interesting events is made by a two-tiered decision-making system: the trigger. The trigger's first part is the hardware-based Level-1 trigger (L1T), which reduces the output to a maximum rate of about 100 kHz. The next trigger level, the software-based High Level Trigger (HLT), decreases the event-rate to several 100 Hz.

The L1T has to decide within 4 µs if an event should be forwarded to the HLT or if it should be already rejected at this stage. This relative long time span for the trigger to make a decision is reached through a pipelined trigger processing and readout architecture that makes concurrent processing of data from several bunch crossings possible. The L1T architecture consists of two main systems, the calorimeter trigger and the muon trigger. The input to the calorimeter trigger comes from the HCAL and the ECAL. The muon trigger combines the information of the three different (partially overlapping) muon systems. The whole information from the calorimeter and muon trigger is forwarded to the Global Trigger (GT), which decides, having all the information from the subsystems, if the event should be looked at in more detail by the HLT or not. The decision of the L1T is mainly based on the location, on p_{T} and on E_{T} of a trigger object, for muons also charge and quality information are available. The logic of the selection of the trigger objects is largely programmable [20, 21, 22].

If an event made it through the L1T, it then has to withstand the sophisticated HLT algorithms to be finally selected for permanent storage. The hardware used for the HLT is a processor farm composed of commodity computers. The processing is organised in paths and the final trigger decision is made by a logical combination of a collection of different paths, this collection is denoted as HLT menu. Each path can contain several steps of filtering and reconstruction modules that have access to the complete read-out data of the L1T. The data accepted by the HLT is then stored permanently and is distributed to several computing centers around the world, which make the data available for physics analysis.

3.6 Detector performance

The LHC was designed for an instantaneous luminosity of $10^{34}\,\mathrm{cm}^{-2}\,\mathrm{s}^{-1}$, but after the upgrade for Run 2, an instantaneous luminosity of $2.06 \times 10^{34}\,\mathrm{cm}^{-2}\,\mathrm{s}^{-1}$

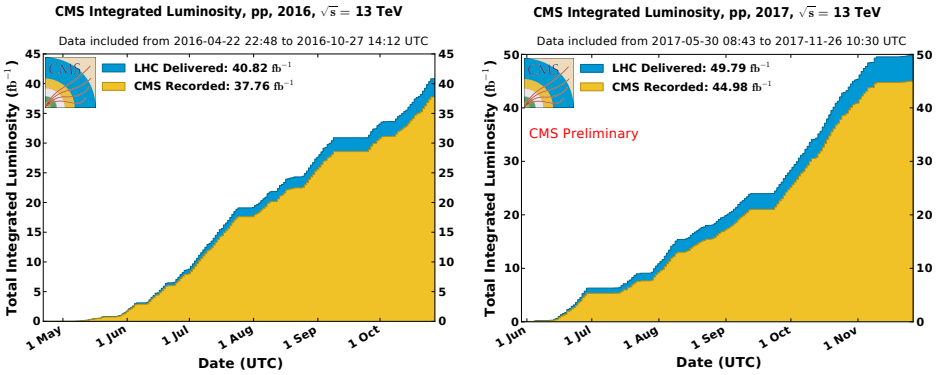

(a) (b)

Figure 5: Integrated LHC offline luminosities for 2016 (a) and 2017 (b) data taking. The recorded luminosity of CMS is also shown. From Ref. [24].

(twice the nominal value) with a maximum of 60 superimposed collisions at one bunch crossing was reached in 2017 [23].

In the years 2016 and 2017 the LHC delivered an integrated luminosity of $40.82\,\text{fb}^{-1}$ and $49.79\,\text{fb}^{-1}$ for pp collisions at $\sqrt{s} = 13\,\text{TeV}$. Thereof CMS recorded $37.76\,\text{fb}^{-1}$ and $44.98\,\text{fb}^{-1}$, respectively. In 2016 the average pileup reached already a value of 27 and increased to a value of 33 in 2017 [24]. The evolution of the integrated luminosities throughout the years 2016 and 2017 is shown in Fig. 5. The aim of the LHC for 2018 is to deliver a luminosity of $60\,\text{fb}^{-1}$, which is about 20% more than in 2017 [25]. At the moment of writing the average pileup of the current 2018 data taking period was 38 and the CMS detector recorded already an integrated luminosity of nearly $50\,\text{fb}^{-1}$ [24].

Chapter 4

Quarkonium

This chapter first introduces the standard model of particle physics which builds the base for further considerations. Then, quarkonia, mesons of a heavy quark and antiquark and their production and polarization are discussed in Sections 4.2, 4.3 and 4.4. The chapter concludes with an overview of the current state of research, giving special attention to bottomonium.

4.1 Standard model of particle physics

Today, the established model for describing the elementary particles and their interactions is the standard model of particle physics. The SM describes three of the four known fundamental forces: the electromagnetic force, the weak force and the strong force. The force not included in the SM is the gravitational force. There are twelve fundamental fermions, six quarks and six leptons, which are grouped into three generations or families. The quarks appear in six flavors: up, down, charm, strange, top, and bottom, where the up, the charm, and the top have an electric charge of $2/3$ (in units of the elementary charge $q = 1.602 \times 10^{-19}\,\mathrm{C}$) and the down, the strange, and the bottom of $-1/3$. Quarks are sensitive to all three forces in the SM. The three charged leptons, the electron (e), the muon (μ), and the tauon (τ) have an electric charge of -1 and can interact through the electromagnetic and the weak force, whereas the three uncharged leptons, the neutrinos, feel only the weak force. For each of these particles also an antiparticle with opposite electric charge exists. In the SM the interaction between particles takes place by the exchange of so called force carrier particles (also denoted gauge bosons):

- eight gluons carry the strong force,
- the massive W^+, W^- and Z^0 bosons mediate the weak force and
- the photon is responsible for the electromagnetic interaction between particles.

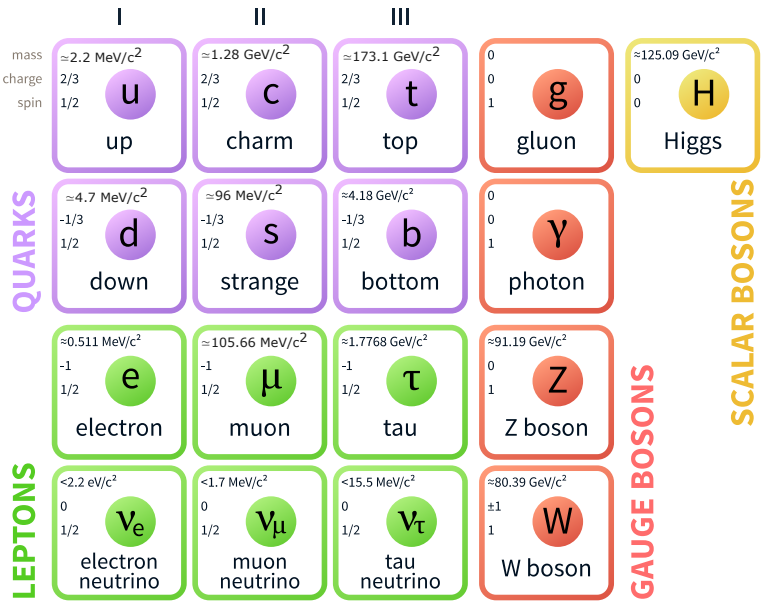

Figure 6: The elementary particles of the SM with their mass, charge and spin. The numbers I, II, and III denote the generation. Adapted from Ref. [26]

An overview of the fundamental particles of the SM as well as their properties is given in Fig. 6.

The mathematical formulation of the SM is based on symmetries. Symmetries have a great importance in physics, since, according to Emmy Noether's theorem [27], there is a corresponding conservation law for every continuous symmetry. So if, for example, a system is symmetric under spatial translation, its momentum is conserved. The SM is gauge invariant (symmetric) under SU(3) $\times$ SU(2) $\times$ U(1) transformation, where the electromagnetic and the weak, the electroweak, interaction is described by a local SU(2) $\times$ U(1) symmetry and the strong interaction by a local SU(3) symmetry. This local gauge invariance is reached with the help of gauge fields. With the introduction of the gauge fields the gauge bosons arise. While the photon and the gluons are massless, the other gauge bosons, the W^+, W^- and Z^0, are massive. To give mass to the W^+, W^- and Z^0 bosons, the electroweak SU(2) $\times$ U(1) symmetry has to be broken spontaneously, which is referred to as Higgs mechanism. By applying the Higgs mechanism another particle, the scalar Higgs boson, whose properties can be found in Fig. 6, emerges.

The SM is a quantum field theory, so its dynamics can be described by a Lagrangian density $\mathscr{L}$. The Lagrangian density of the standard model includes terms for the gauge fields, dynamical and mass terms for the quarks and leptons and dynamical and mass terms for the Higgs boson. The sector of the SM describing the strong interaction of quarks and gluons, and

hence the dynamics of quarkonium, is quantum chromodynamics (QCD). Its Lagrangian density is given by [28]

$$\mathscr{L}_{\mathrm{QCD}} = \underbrace{-\frac{1}{4}\sum_{a=1}^{8} G^a_{\mu\nu} G^{a\mu\nu}}_{\mathscr{L}_{\mathrm{gluon}}} + \underbrace{\sum_{f=1}^{6} [\bar{\mathbf{q}}_f \mathrm{i}\gamma^\mu (\partial_\mu + \mathrm{i}g\mathbf{G}_\mu)\mathbf{q}_f - m_f \bar{\mathbf{q}}_f \mathbf{q}_f]}_{\mathscr{L}_{\mathrm{quark}}}, \quad (4.1)$$

where $\mathbf{G}_\mu$ is the 3×3 matrix gauge field that is responsible for the local SU(3) symmetry of the SM. Under a local SU(3) transformation, $\mathbf{U}$, $\mathbf{G}_\mu$ behaves as

$$\mathbf{G}_\mu \to \mathbf{G}'_\mu = \mathbf{U}\mathbf{G}_\mu\mathbf{U}^\dagger + (\mathrm{i}/g)(\partial_\mu \mathbf{G}_\mu)\mathbf{G}^\dagger_\mu.$$

The $G^a_{\mu\nu}$ in Eq. 4.1 are the components of the Yang-Mills construction [29], $\mathbf{G}_{\mu\nu}$, which is given by

$$\mathbf{G}_{\mu\nu} = \partial_\mu \mathbf{G}_\nu - \partial_\nu \mathbf{G}_\mu + \mathrm{i}g(\mathbf{G}_\mu \mathbf{G}_\nu - \mathbf{G}_\nu \mathbf{G}_\mu).$$

For each flavor f of quarks, there is a field for each of the three color states r, g and b, these fields are put into color triplets $\mathbf{q}_f$:

$$\mathbf{q}_f = \begin{pmatrix} \mathrm{q}_{f,\mathrm{r}} \\ \mathrm{q}_{f,\mathrm{g}} \\ \mathrm{q}_{f,\mathrm{b}} \end{pmatrix}.$$

Each component of such a color triplet is a four-component Dirac spinor. The γ^μ are the Dirac gamma matrices, which are also used to define $\bar{\mathbf{q}}_f = \mathbf{q}^\dagger_f \gamma_0$. The parameter g in Eq. 4.1 is the strong coupling (often given as $\alpha_\mathrm{s} = g^2/(4\pi)$). The strength of the coupling depends on the momentum transfer P^2, which is denoted as running coupling strength. In contrast to QED, where the strength of the coupling increases with increasing energy, in QCD $\alpha_\mathrm{s}(P^2)$ decreases with increasing P^2, thus for small distances. This leads to the phenomenon of asymptotic freedom at distances below about 0.2 fm, where the quarks and gluons can be considered to behave like free particles. With increasing distances the coupling gets stronger and leads to confinement. Because of confinement neither free quarks nor free gluons have been observed so far and only color-neutral combinations of quarks are experimentally observable. The coupling for large P^2 (at lowest order modifications caused by vacuum polarization) is given by [28]

$$\alpha_\mathrm{s}(P^2) = \frac{4\pi}{[11 - (2/3)n_f] \ln(P^2/\Lambda^2_{\mathrm{QCD}})}, \quad (4.2)$$

where n_f is the effective number of quark flavors and $\Lambda_{\mathrm{QCD}} \sim 0.2\,\mathrm{GeV}$ is the characteristic energy scale of QCD. As can be seen in Eq. 4.2, $\alpha_\mathrm{s}(P^2) \to 0$ for $P^2 \to \infty$.

4.2 Quarkonium physics

Quarkonia are bound states of a heavy quark Q and a heavy antiquark $\bar{Q}$ of the same flavor. The term heavy refers to the large masses of the charm, the bottom and the top quark, $m_Q \gg \Lambda_{\mathrm{QCD}}$, in contrast to the light up, down and strange quark, $m_q \ll \Lambda_{\mathrm{QCD}}$. However, only c and b quarks can form bound states since the top quark decays before a bound state can be formed. The bound $c\bar{c}$ and $b\bar{b}$ systems are referred to as charmonium and bottomonium. The first discovery of a charmonium state at 3.1 GeV was made in 1974 in Brookhaven and SLAC [30, 31], where the first group named the found resonance ψ and the other J, so that now the particle is known as J/ψ. The first observation of a bottomonium state, the $\Upsilon(1S)$ at 9.5 GeV, was reported in 1977 at Fermilab [32]. Just like positronium (a bound system of an electron and a positron) serves as a laboratory for making precision tests to check and confirm quantum electrodynamics (QED) to high precision [33], quarkonium has a high potential for answering open questions concerning QCD [34, 35]. For example, quarkonium is an ideal system to study hadronization, the process of the formation of bound states of quarks and gluons by the strong interaction.

Quarkonia are multiscale systems, characterized by their constituents' average relative velocity, v^2, which is $v^2 \sim 0.1$ for bottomonium and $v^2 \sim 0.3$ for charmonium [35]. There are three distinct energy scales for quarkonium [36]:

- the mass m_Q of the heavy quark - *hard scale*,
- the relative momentum $m_Q v$, corresponding to the inverse Bohr radius $r \sim 1/(m_Q v)$ (the size of the bound state) - *soft scale*,
- the typical kinetic energy $m_Q v^2$ (the inverse gives the typical time scale) - *ultrasoft scale*.

The production of quarkonium, which is discussed in Section 4.3, takes place at the hard scale, the binding process is a phenomenon of the soft scale, and very low-energy gluons in the ultrasoft scale are responsible for effects like the Lamb shift in QCD. For quarkonia the hard, soft, and ultrasoft scale are widely separated and the following hierachy holds: $m_Q v^2 \ll m_Q v \ll m_Q$. Because of this different and widespread energy scales of quarkonia, observables of a particular energy region can be described by integrating out the other energy scales, which is the basic idea of effective field theories (EFTs) such as nonrelativistic QCD (NRQCD) [37] or potential NRQCD (pNRQCD) [38]. Another important scale, already introduced in Eq. 4.2, at which nonperturbative effects have to be considered is Λ_{QCD}.

These distinct scales of quarkonium makes it an ideal system to probe QCD in regimes where perturbative calculations are applicable as well as

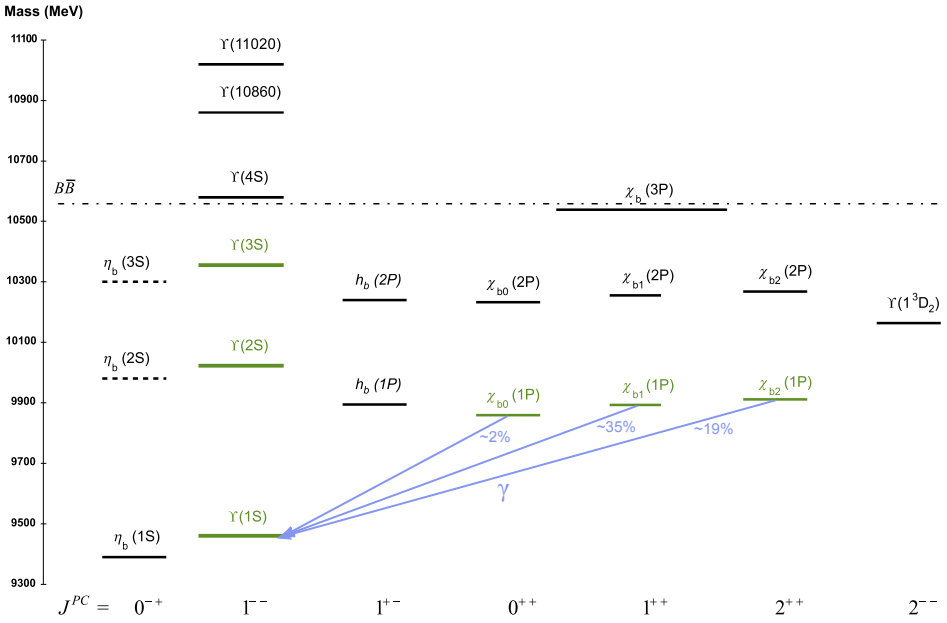

Figure 7: The energy levels of experimentally established bottomonium states. In parantheses the radial quantum number and the orbital angular momentum are given (e.g. 1P stands for $n = 1$ and $L = 1$). The dash-dotted line marks the open bottom $B\bar{B}$ threshold. The states important for this work are colored green. The blue arrows show the radiative transition of the $\chi_{\mathrm{b}J}(1\mathrm{P})$ states into the $\Upsilon(1\mathrm{S})$ state and the corresponding decay probabilities. Adapted from [39]

at regimes where not. Thus, quarkonium serves as an excellent testing area for gaining a better understanding of the interplay between these different regimes.

A quarkonium state, $\mathcal{Q}$, can be characterized by the principal quantum number n, the total spin S (0 or 1), the orbital angular momentum L and the combination of S and L in the total angular momentum $\vec{J} = \vec{L} + \vec{S}$, whose magnitude J fulfills $|L - S| \leq J \leq L + S$. There are two other important properties to describe a quarkonium state: parity $P = (-1)^{L+1}$ and charge conjugation $C = (-1)^{L+S}$, from which L and S can be derived when also J is measured. There are two possibilities of fully declaring a quarkonium state: either with the spectroscopic notation $n^{2S+1}L_J$ or in the form J^{PC}. In Fig. 7 and Fig. 8 all currently experimentally established bottomonium and charmonium states are shown. The open bottom ($B\bar{B}$) and charm ($D\bar{D}$) thresholds in the figures mark the energy that is needed to build a bound state of two B mesons, $B\bar{B}$, or two D mesons, $D\bar{D}$. B and D mesons are mesons of a heavy bottom or charm quark, respectively, bound with a light up or down quark. The bottomonium states important

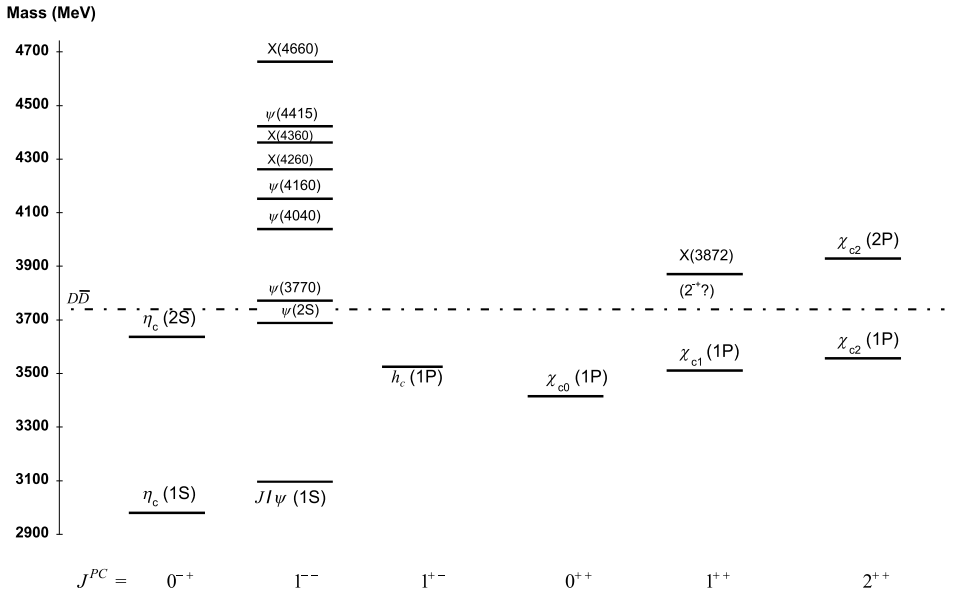

Figure 8: The energy levels of experimentally established charmonium states. States that are not yet identified as a $c\bar{c}$ state are denoted with X. In parantheses the radial quantum number and the orbital angular momentum are given. The dash-dotted line marks the open-charm threshold $D\bar{D}$. Adapted from [39]

Table 1: Masses, widths and quantum numbers of bottomonium states relevant for this thesis.

State	Mass (MeV)	Full width (keV)	J^{PC}	S	L
Υ(1S)	9460.30 ± 0.26	54.02 ± 1.25	1^{--}	1	0
χ_{b0}(1P)	9859.44 ± 0.73	-	0^{++}	1	1
χ_{b1}(1P)	9892.78 ± 0.57	-	1^{++}	1	1
χ_{b2}(1P)	9912.21 ± 0.57	-	2^{++}	1	1
Υ(2S)	$10\,023.26 \pm 0.31$	31.98 ± 2.63	1^{--}	1	0
Υ(3S)	$10\,355.2 \pm 0.5$	20.32 ± 1.85	1^{--}	1	0

for this thesis are the χ_{bJ}(1P) with $L = S = 1$ and $J = 0, 1, 2$ as well as the Υ(1S) with $L = 0$ and $J = S = 1$. In Fig. 7 also the radiative transitions from the χ_{bJ}(1P) states to the Υ(1S) state and the corresponding decay probabilities are shown, as these radiative decays to the Υ(1S) state are used to reconstruct the χ_{bJ}(1P) mesons in this work. In Table 1 the masses, widths and quantum numbers of the bottomonium states relevant for this thesis are listed.

In particle detectors quarkonia are detected through their decay in a pair of muons or electrons. At the CMS detector, the decay, ψ(nS)/Υ(nS) $\rightarrow$ $\mu^+\mu^-$ provides the cleanest signature for measuring S-wave state quarkonia. Of all produced Υ(1S) particles only a fraction of about 2.5% decay into a pair of muons [39]. The P-wave states are measured through their radiative decay to an S-wave state and the subsequent decay of the S-wave state to a dimuon: $\chi_{\{b,c\}J} \rightarrow \mu^+\mu^-\gamma$. The χ_{b1}(1P) and χ_{b2}(1P) states decay in about 35 and 19 % of the cases to the Υ(1S) [39].

4.3 Quarkonium production

The production of particles in hadron collisions can be described in terms of the interactions between the quarks and gluons, the partons, inside the colliding hadrons. Because of their high mass, the heavy quarks are initially produced in partonic collisions with high momentum transfer and thus can be treated perturbatively. The subsequent quarkonia formation out of two heavy quarks has then to be treated nonperturbatively. There are several models describing quarkonium production in hadron-hadron collisions. At the moment the most discussed one is the NRQCD factorization approach, which is introduced in the next section. Other approaches are k_T factorization [40], the color singlet model (CSM) [41], which is a special case of the NRQCD factorization, or the color evaporation model (CEM) [42].

A certain quarkonium state can be produced directly or stem from ra-

diative or hadronic transitions of higher states. These so called feed-down contributions from higher states play an important role in the analysis of quarkonium, hence, a proper understanding of them is crucial. Especially for the S-wave states the contribution from the P-wave states is important since they have different quantum numbers. The distributions of other S-wave states should have the same polarization. Another contribution to the total cross section for charmonium mesons comes from weak decays of the heavier B mesons, which is, because of the lifetime of these mesons, denoted as nonprompt production.

4.3.1 NRQCD factorization approach

Since the relative velocity in quarkonia is small, $v \ll 1$, a nonrelativistic description of the hadronization is possible. Caswell and Lepage were the first to propose a general procedure for studying nonrelativistic systems in any relativistic field theory [43]. To obtain such a nonrelativistic theory the relativistic theory has to be transformed by integrating out all quantum fluctuations at momentum scales of order m or larger [44]. In this way NRQCD is obtained by integrating out the scale m_Q from QCD. Going one step further, additionally integrating out the scale $m_Q v$ from NRQCD, one produces potential NRQCD (pNRQCD) [38]. In Fig. 9 a schematic overview of the energy scales of quarkonia and the corresponding EFTs is given. Bodwin, Braaten, and Lepage then developed a general factorization approach for heavy quarkonium production within NRQCD [37], where the production process is separated into a perturbative and a nonperturbative part.

The cross section σ in the NRQCD factorization formalism for the production of a quarkonium state $\mathcal{Q}$ (plus other particles X) in the collision of the systems A and B is

$$\sigma(A+B \to \mathcal{Q}+X) = \sum_{S,L,\mathrm{c}} \mathcal{S}(A+B \to Q\bar{Q}[^{2S+1}L_J^{[\mathrm{c}]}]+X) \times \mathcal{L}(Q\bar{Q}[^{2S+1}L_J^{[\mathrm{c}]}] \to \mathcal{Q}), \tag{4.3}$$

where the sum goes over various angular momentum configurations, (L, S), and the color-multiplicity c. The short-distance coefficient (SDC), $\mathcal{S}$, is proportional to the parton cross section of the initial $Q\bar{Q}$ pair and can be calculated perturbatively. The nonperturbative long-distance matrix elements (LDMEs), $\mathcal{L}$, which are constrained by experimental data, are proportional to the probability that the initial pair evolves into a certain bound state $\mathcal{Q}$. In contrast to the SDCs, which are dependent on the production process, the LDMEs are assumed to be universal, which means that they are independent of the process $A + B$ that created the initial heavy quarks. In general, to calculate the full cross section, the sum in Eq. 4.3 would have to be built over all possible quantum states. But, the magnitude of the LDMEs

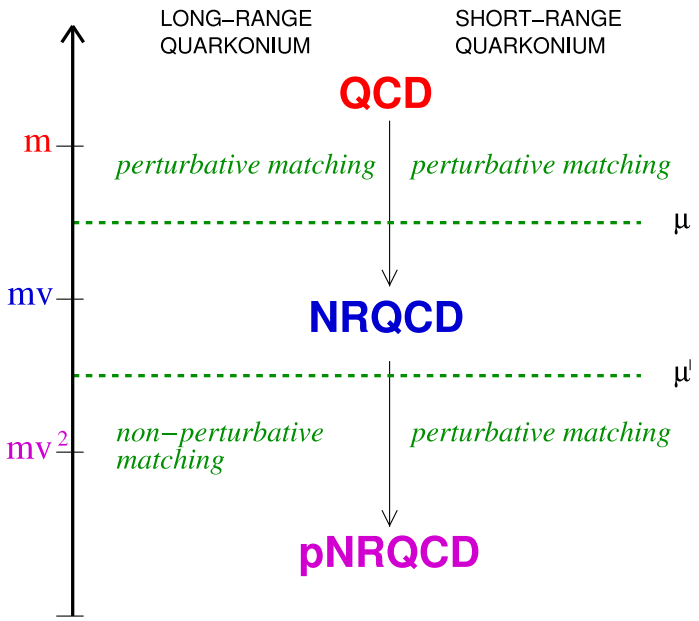

Figure 9: Energy scales and corresponding EFTs. For the short-range quarkonia a perturbative treatment of the scale mv is allowed, for the long range quarkonia a nonperturbative treatment of this scale is required. The scale μ separates QCD from NRQCD and the scale μ' separates NRQCD from pNRQCD. From Ref. [36]

of a specific intermediate state can be ordered in powers of the heavy quark velocity v. Thus, only a finite number of terms contribute to Eq. 4.3 for calculations up to a specific order in v. However, there are no general rules on how to assign these hierarchies. Different possibilities for the scaling of the LDMEs with v are discussed in Ref. [45].

The initial $Q\bar{Q}$ pair is allowed to have color charge before it turns into the physically observable color-neutral quarkonium state $\mathcal{Q}$. It is important not to forget that the LDMEs and the SDCs of a given term in expansion are, not observable individually and that the extraction of the LDMEs requires the knowledge of the SDC functions [46]. Hence, it makes a difference for the value of the LDMEs wheter the SDC was perturbatively calculated only at leading order (LO) or at next-to-leading order (NLO). An example for a differential cross section calculated at NLO for the J/ψ is shown in Fig. 10. The figure also shows the individual contributions taken into account: the color-singlet term ${}^3\mathrm{S}_1^{[1]}$ and the color-octet terms ${}^3\mathrm{S}_0^{[8]}$, ${}^3\mathrm{S}_1^{[8]}$, and ${}^3\mathrm{P}_J^{[8]}$.

Further details on the factorization approach in NRQCD can be found in Ref. [37].

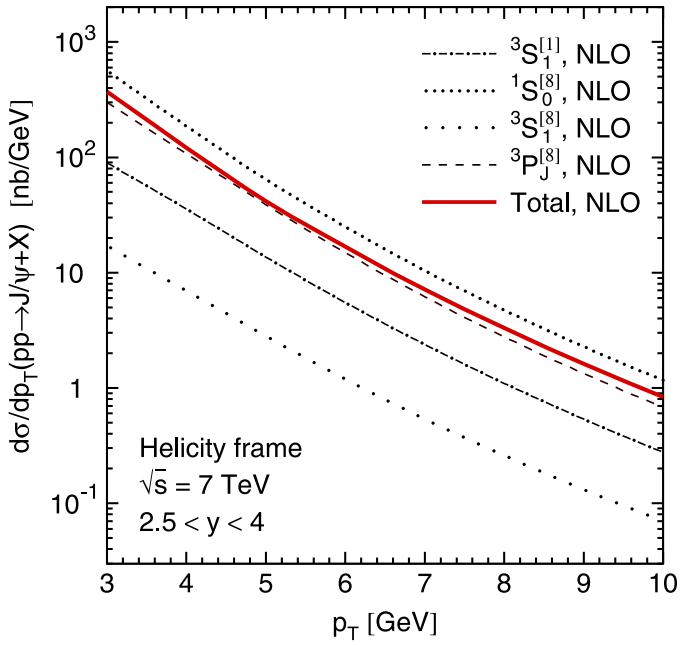

Figure 10: An example for a differential cross section for the J/ψ calculated at NLO with NRQCD factorization, also showing the individual contributions of the color-singlet and color-octet terms. The $^3P_J^{[8]}$ color-octet gives a negative contribution. From Ref. [47].

4.4 Quarkonium polarization

The polarization denotes which angular momentum component $J_z = \{-J, -J+1, ..., J\}$ of the $b\bar{b}$ or $c\bar{c}$ mesons is preferred. For the vector quarkonia ($J^{PC} = 1^{--}$) the two extreme cases of fully longitudinal, $J_z = \pm 1$, or fully transversal, $J_z = 0$, polarization can be distinguished. Of course, also a superposition of the different J_z states with just a slight preference for a specific direction is possible. In the case that each J_z state is equally likely, the quarkonium state is said to be unpolarized. It is important to be aware that the polarization is always defined with respect to a specific quantization axis z.

Since quarkonia cannot be observed directly, their properties, such as the polarization, have to be deduced from the measured decay products. This is possible considering angular momentum conservation and basic symmetries of the interaction that is responsible for the decay. The following discussion shows how the preferred J_z alignment of a quarkonium state can be determined from the angular decay distribution.

For vector quarkonia the angular decay distribution of the lepton pairs

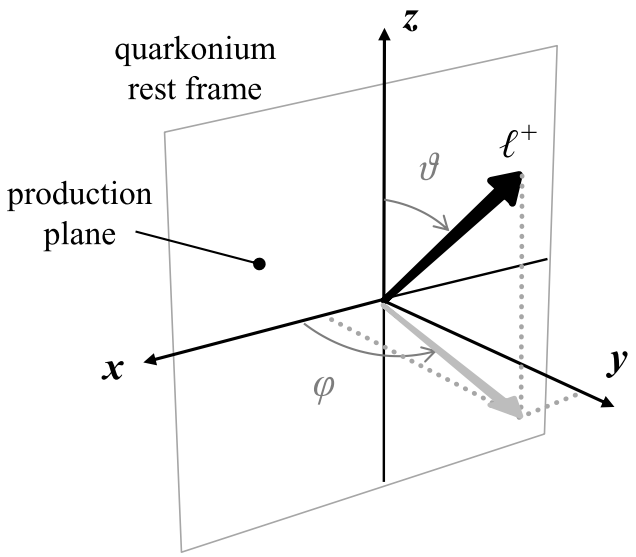

Figure 11: The azimuthal angle φ and the polar angle ϑ of the positively charged lepton ℓ^+ in the quarkonium rest frame [48].

in the quarkonium rest frame is given by

$$W(\cos\vartheta, \varphi|\vec{\lambda}) \propto \frac{1}{3+\lambda_\vartheta}(1 + \lambda_\vartheta \cos^2\vartheta + \lambda_\varphi \sin^2\vartheta \cos 2\varphi + \lambda_{\vartheta\varphi} \sin 2\vartheta \cos\varphi), \tag{4.4}$$

where φ and ϑ are the azimuthal and polar angles of the positively charged lepton ℓ^+ in the quarkonium rest frame and $\vec{\lambda} = (\lambda_\vartheta, \lambda_\varphi, \lambda_{\vartheta\varphi})$ represents the polarization parameters [48]. The definitions of ϑ and φ are shown in Fig. 11. Integrating Eq. 4.4 over φ or over $\cos\vartheta$ gives the one-dimensional distributions $W(\varphi)$ and $W(\cos\vartheta)$:

$$W(\cos\vartheta|\vec{\lambda}) \propto \frac{1}{3+\lambda_\vartheta}(1 + \lambda_\vartheta \cos^2\vartheta) \tag{4.5}$$

and

$$W(\varphi|\vec{\lambda}) \propto 1 + \frac{2\lambda_\varphi}{3+\lambda_\vartheta} \cos 2\varphi. \tag{4.6}$$

The parameters $\vec{\lambda}$ depend on the definition of the coordinate system in the quarkonium rest frame, in which the angular decay distribution is measured. Different choices for the axes lead to different shapes of the the one-dimensional distributions $W(\varphi)$ and $W(\cos\vartheta)$ and to different values for $\vec{\lambda}$.

The x and z axes of the coordinate system can be chosen freely within the production plane, i.e. the plane spanned by the colliding beams and

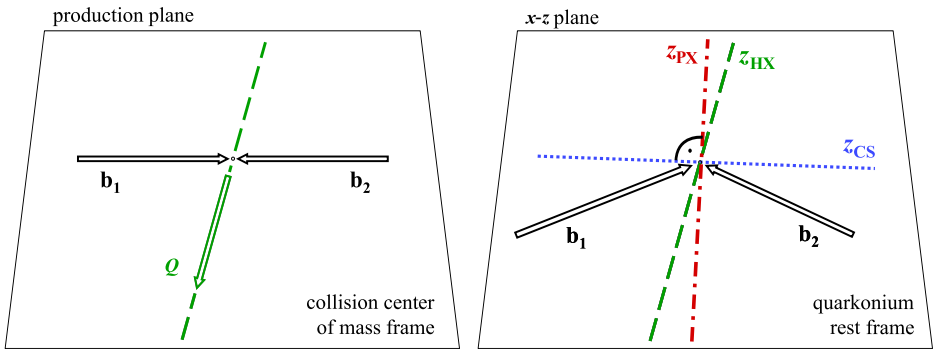

Figure 12: The production plane in the collision centre-of-mass frame (left) and in the quarkonium rest frame (right). $\mathbf{b}_1$ and $\mathbf{b}_1$ denote the beam vectors. On the right the z-axes of the PX, HX and CS frames are shown. Adapted from [48].

the produced quarkonium, as shown in Fig. 12. The y axis is always perpendicular to the production plane. One common choice to define the z axis is the so called helicity (HX) frame. In that frame the z axis is defined in the flight direction of the quarkonium in the collision center-of-mass (also called laboratory) frame. Another possibility is the Collins-Soper (CS) frame, where the bisector of the angle of one beam and the opposite of the other beam in the dimuon rest frame defines the z direction. The frame that has the z axis defined perpendicular to the one in the CS frame, is called perpendicular-helicity (PX) frame.

That there are several reference frames, which lead to different polarization parameters, can complicate the comparison of results from different analyses and hence lead to confusion. It is possible to find combinations of λ_ϑ, λ_φ and $\lambda_{\vartheta\varphi}$ that give the same result, independent of the frame in which the parameters were measured. One often used frame-invariant parameter $\tilde{\lambda}$ is defined as

$$\tilde{\lambda} = \frac{\lambda_\vartheta + 3\lambda_\varphi}{1 - \lambda_\varphi}. \tag{4.7}$$

An advantage is that $\tilde{\lambda}$ can be used to probe systematic effects due to experimental biases by comparing $\tilde{\lambda}$ determined from at least two orthogonal frames [48].

It was shown in Ref. [49], that the polarization of a χ state that decays as $\chi_{\mathrm{b}}(\chi_{\mathrm{c}}) \to \Upsilon(J/\psi)\gamma$ can be determined from a measurement of the polarization of the Υ or the J/ψ. If then the decay $\Upsilon(J/\psi) \to \ell^+\ell^-$ follows, which is the case in this analyis, the same formalism described before can be applied. When using this method it is important to have in mind that there are some constraints that have to be satisfied. The lepton pairs $\ell^+\ell^-$ have to have sufficiently high momentum that the dilepton angular distribution

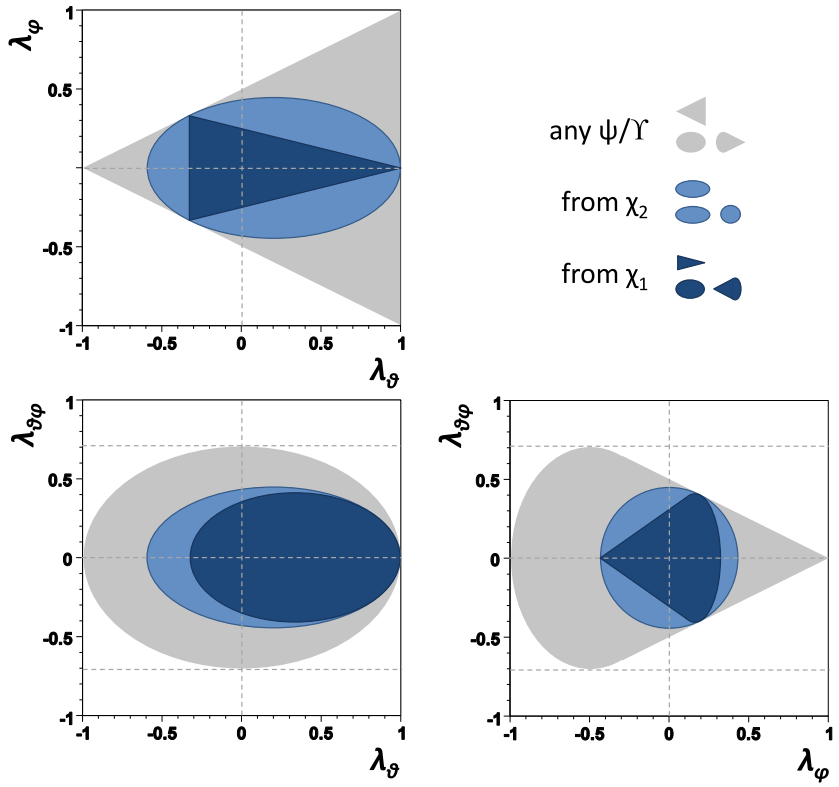

Figure 13: Allowed regions for the angular parameters. For the Υ(nS) or the ψ(nS) the allowed values for λ_ϑ, λ_φ and $\lambda_{\vartheta\varphi}$ have to lie within the grey area. If these S-wave states originate from χ_1 or χ_2 radiative decays, they have to lie within the dark or light blue area, respectively. From Ref. [49].

can be used to directly determine the χ polarization. Further, the photon momentum is ignored, which is only valid for the domain where $p_{\mathrm{T}} \gg \Delta M$, where ΔM is the mass difference of the χ and the vector quarkonium. The error of the polarization parameter λ_ϑ of the χ state is given by [49]

$$\left|\frac{\Delta\lambda_\vartheta}{\lambda_\vartheta}\right| = \mathcal{O}\left[\left(\frac{\Delta M}{p}\right)^2\right], \tag{4.8}$$

where p is the momentum of the dilepton in the laboratory frame. It can also be shown that the polarization parameters of the dilepton distribution have to satisfy characteristic inequalities [49]. The ranges that arise from these inequalities are shown in Fig. 13.

Fortunately, the condiditions of the measurements used in this thesis fulfill these constraints: Taking the masses of the $\chi_{\mathrm{b}2}(1\mathrm{P})$ and the $\Upsilon(1\mathrm{S})$ from the Particle Data Group (PDG) [39] one gets already for $p > 5\,\mathrm{GeV}$, which is always the case in this analysis, an error smaller than 1%.

4.5 Current experimental status

An important topic in the field of bottomonium research is the exact measurement of the feed-down fractions. Since the contributions from higher P-wave states could significantly influence the polarization of the Υ states, a precise knowledge of them is important for the comparison to theory predictions.

The most recently discovered P-wave state is the $\chi_{\mathrm{b}}(3\mathrm{P})$, whose discovery was first reported by ATLAS in 2011 [50]. Shortly thereafter the D0 collaboration also observed this state [51]. Both groups identified the $\chi_{\mathrm{b}}(3\mathrm{P})$ state through its radiative decay to the $\Upsilon(1\mathrm{S})$ state. The ATLAS collaboration additionally measured the decay into the $\Upsilon(2\mathrm{S})$ state. These measurements could not yet distinguish the individual $\chi_{\mathrm{b}J}(3\mathrm{P})$ states of the multiplet. The first observation of the distinct $\chi_{\mathrm{b}1}(3\mathrm{P})$ and $\chi_{\mathrm{b}2}(3\mathrm{P})$ peaks and the measurement of their mass difference was reported only recently by the CMS collaboration [52]. The measurement was based on data collected at the CMS detector from 2015 to 2017 at $\sqrt{\mathrm{s}} = 13\,\mathrm{TeV}$. A mass splitting of $m_{\chi_{\mathrm{b}2}(3\mathrm{P})} - m_{\chi_{\mathrm{b}1}(3\mathrm{P})} = 10.61\,\mathrm{MeV}$, as well as a mass of $10.513\,\mathrm{GeV}$ for the $\chi_{\mathrm{b}1}(3\mathrm{P})$ state was determined. In Fig. 14 the invariant mass distribution of the $\mu^+\mu^-\gamma$ system used for this measurement are shown. The peaks of the $\chi_{\mathrm{b}1}(3\mathrm{P})$ and $\chi_{\mathrm{b}2}(3\mathrm{P})$ states can clearly be distinguished.

The latest measurements of radiative feed-down contributions from χ_{b} to Υ states were made by LHCb with data samples collected at $\sqrt{\mathrm{s}} = 7\,\mathrm{TeV}$ and $\sqrt{\mathrm{s}} = 8\,\mathrm{TeV}$ [53]. For the radiative decay $\chi_{\mathrm{b}}(1\mathrm{P}) \to \Upsilon(1\mathrm{S})\gamma$ they measured fractions of about 15 to 30 % which are increasing with the transverse momentum of the Υ. The measurements were performed in a p_{T} range from 6 to 40 GeV and an absolute rapidity of $2 < |y| < 4.5$. They measured also

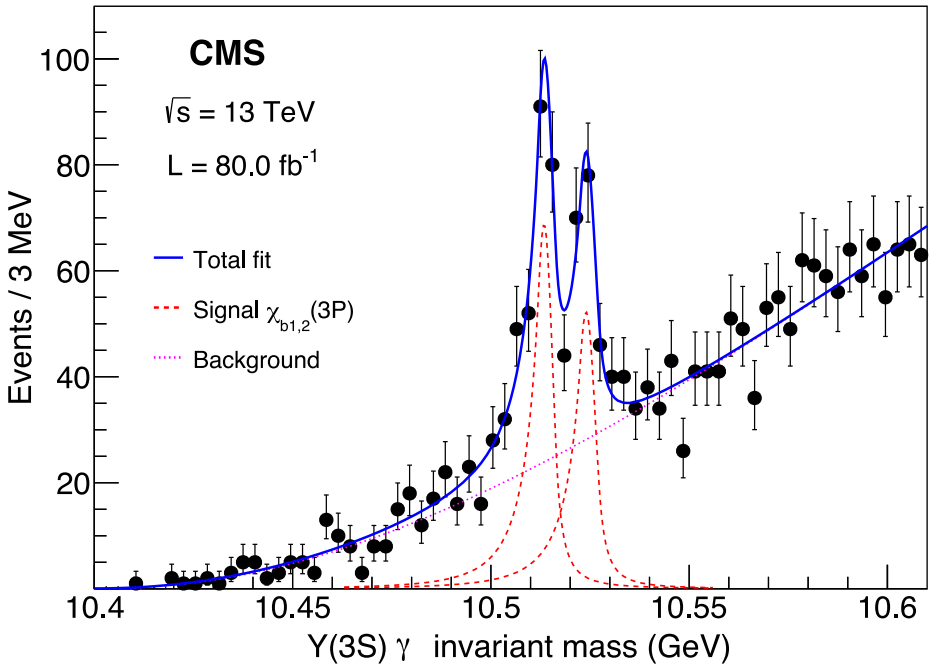

Figure 14: The invariant mass distribution of the $\chi_{bJ}(3P) \to \Upsilon(3S)\gamma$ candidates. The $\chi_{b1}(3P)$ (left) and $\chi_{b2}(3P)$ (right) peaks can clearly be distinguished. From Ref. [52].

the fraction of $\chi_b(3P)$ decaying to $\Upsilon(nS)$ and the fraction of $\chi_b(2P)$ decaying to the $\Upsilon(2S)$ and $\Upsilon(1S)$ states. An earlier measurement of the feed-down contributions for the radiative decays from the $\chi_b(1P)$ and the $\chi_b(2P)$ to the $\Upsilon(1S)$ state were reported by the Collider Detector at Fermilab (CDF) collaboration in 2000 [54].

For the verification of theoretical predictions for high-energy hadron collisions, quarkonium polarization measurements are eligible. The most recent publication of the Υ polarization comes from LHCb [55]. Before, also the CMS [56] and CDF [57] collaborations made measurements of the Υ polarization. The measurements were made in different rapidity regions as a function of the transverse momentum. In all regions a nearly isotropic angular distribution of the decay muons was reported by all three groups. The results are in disagreement with theoretical expectations for high-energy hadron collisions [56]. In Fig. 15 the polarization parameters λ_ϑ in the HX frame determined from the CMS and CDF measurements are shown for different rapidity regions.

This section presented recent measurements of the Υ polarization as well as feed-down studies for the bottomonium, which report that $30 - 40\%$ of the Υ states originate from higher χ_b states. Consequently the polarization

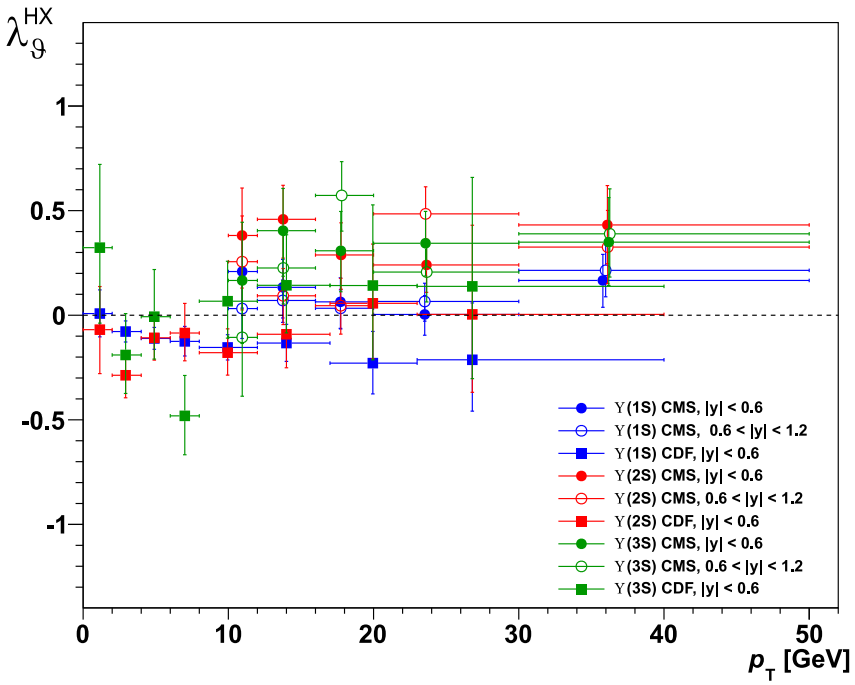

Figure 15: Compilation of the results of the Υ polarization measurements from CMS [56] and CDF [57] for different rapidity regions as a function of p_{T}.

of the χ_{b} states can have a not negligible influence on the polarization of the Υ states. Therefore, the knowledge of the polarization of the quarkonium P-wave states is of great importance and might help to understand the disagreement of the measured Υ polarization with theoretical predictions. So far no measurements of the polarization of any χ_{b} state were performed. This work will provide first results of the relative $\chi_{\mathrm{b2}}(1\mathrm{P})/\chi_{\mathrm{b1}}(1\mathrm{P})$ polarization.

Chapter 5

Data analysis

5.1 Strategy

The aim of this thesis is to obtain first results of the relative polarization of $\chi_{b2}(1P)$ to $\chi_{b1}(1P)$ mesons emerging from high-energy hadron collisions at the LHC, using data taken with the CMS detector in pp collisions at an energy of $\sqrt{s} = 13\,\text{TeV}$ in the years 2016 and 2017. The used data samples of these years correspond to an integrated luminosity of $34.88\,\text{fb}^{-1}$ and $37.15\,\text{fb}^{-1}$, respectively. The $\chi_b(1P)$ candidates are reconstructed through the $\chi_b(1P) \to \Upsilon(1S) \to \mu^+\mu^-\gamma$ decay, where the photon is reconstructed using conversion electrons. More details on the data samples are given in Section 5.2.

The polarization is determined from the preferred direction of the decay muons in the dimuon rest frame, as described in Section 4.4. Its dependence on the angular variables $\cos\vartheta$ and φ is given by Eq. 4.4. In this work the relative polarization of $\chi_{b2}(1P)/\chi_{b1}(1P)$ events is investigated as function of $\cos\vartheta$ in the helicity frame. Only the $\cos\vartheta$ distribution as given in Eq. 4.5 is investigated, since it is assumed that the φ distribution in the helicity frame is flat, which still has to be shown on data.

The angular distribution is very sensitive to effects, such as the trigger efficiency, the acceptance and the reconstruction efficiency, and can change the measured polarization significantly if not considered correctly. For that reason it was decided to study the $\chi_{b2}(1P)/\chi_{b1}(1P)$ ratio, assuming that all these effects as well as unknown detector effects largely cancel out, as will be discussed in more detail in Section 5.5.

To extract the yields of the $\chi_{b1}(1P)$ and the $\chi_{b2}(1P)$ candidates from the full data sample which also contains unwanted background events (which, if they are completely random $\mu^+\mu^-\gamma$ combinations, can have a very different polarization), a fit to the invariant mass distribution of the $\chi_{b1}(1P)$ candidates, hereinafter referred to as $\chi_{b1}(1P)$ mass fit, is performed. The relative $\chi_{b2}(1P)/\chi_{b1}(1P)$ angular distribution is obtained using two differ-

ent approaches, as explained in detail in Section 5.3. The measured relative $\cos\vartheta$ distributions are compared to different scenarios obtained from simulated samples produced with different polarizations. In this way it is tried to exclude some $\chi_{b2}(1P)/\chi_{b1}(1P)$ polarization scenarios.

The only relevant systematic uncertainties in this measurement concern the mathematical model for the $\chi_{b1}(1P)$ mass fit, which is shown in Section 5.5.

5.2 Data and Monte Carlo samples

The data used for this analysis were recorded in the years 2016 and 2017 in pp collisions at an energy of $\sqrt{s} = 13\,\text{TeV}$ at the CMS experiment at the LHC. The $\chi_b(1P)$ particles are observed through their radiative $\chi_b(1P) \to \Upsilon(1S)\gamma$ decay, where the photons are detected in the silicon tracker through their subsequent $\gamma \to e^+e^-$ conversion to an electron-positron pair and the Υ particles through their $\Upsilon(1S) \to \mu^+\mu^-$ decay into two opposite charged muons. Since the p_T of most of the photons coming from $\chi_b(1P) \to \Upsilon(1S)\gamma$ decays is below 2.5 GeV, as shown in Fig. 16, the highest precision of the photon energy is obtained by the detection of the photon through the tracking of the electron-positron pair originating from its conversion. Furthermore, a more accurate determination of the interaction vertex is possible by the detection of the photon conversions in the inner tracker than in the ECAL, which is important for combining the $\Upsilon(1S)$ candidates with the right photons from the same vertex, which consequently leads to less combinatorial background. The downside of the measurement using conversion photons is the small yield due to the small probability of a photon to convert into an electron-positron pair before the last three layers of the inner tracker, which are at least required for the detection of the photons. Before the pixel detector upgrade at the end of 2016, the probability for a conversion to occur early enough to be detected within the CMS detector was about 20 to 40 % in the barrel region of the inner tracker, depending on p_T [58]. After the upgrade, where a fourth layer was added to the pixel detector, the yield should have increased, but so far no updated studies are available.

The HLT paths for this study are called `HLT_Dimuon8_Upsilon_Barrel` for the 2016 and `HLT_Dimuon10_Upsilon_Barrel_Seagulls` for the 2017 data taking period. They recorded an integrated luminosity of $34.88\,\text{fb}^{-1}$ and $37.15\,\text{fb}^{-1}$, respectively. Both trigger paths required the muon pair to have an invariant mass of 8.5 to 11.5 GeV, which is the mass region of the Υ particles, and the χ^2 probability of the dimuon vertex fit to be greater than 0.5 %. The term 'barrel' in the name of the trigger path indicates that the rapidity of the dimuon, $y^{\mu\mu}$, has to fulfill $|y^{\mu\mu}| < 1.25$ to lie within the barrel region of the detector. The main difference between the two HLT paths is that a minimum dimuon transverse momentum, $p_T^{\mu\mu}$, of 7.9 GeV in 2016 and

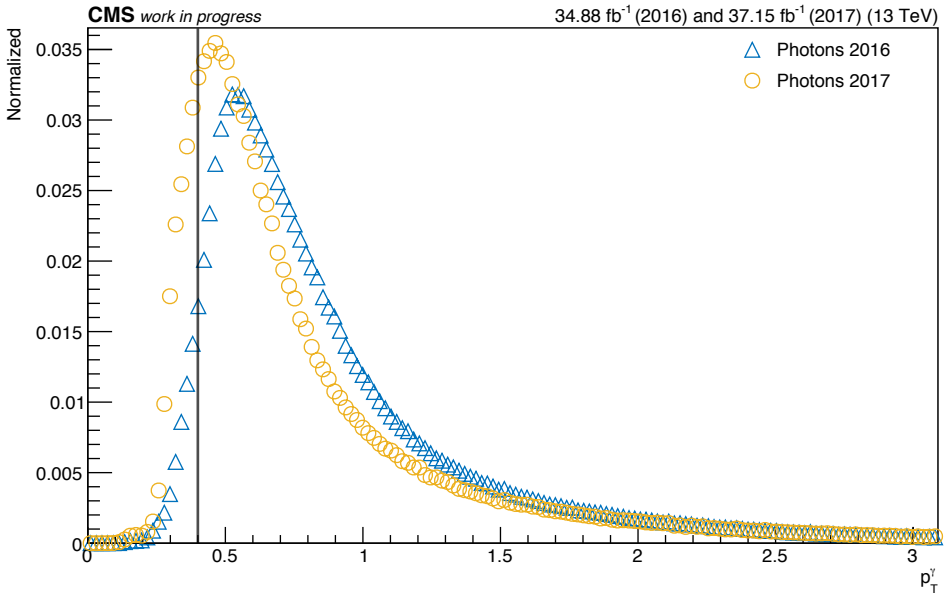

Figure 16: Normalized p_{T} distributions of the photons from $\chi_{\mathrm{b}}(1\mathrm{P}) \to \Upsilon(1\mathrm{S})\gamma$ decays for 2016 (blue) and 2017 (yellow). The straight black line indicates the selection of $p_{\mathrm{T}}^{\gamma} > 0.4\,\mathrm{GeV}$ applied for this analysis.

9.9 GeV in 2017 was required, and that in 2017 only dimuons where the muons bend away from each other, so called seagulls, were recorded. The details of the HLT trigger selection criteria are summarized in Table 2.

The L1 triggers, which seed the HLT, also changed between the two data taking periods. The `HLT_Dimuon8_Upsilon_Barrel` trigger was seeded by two L1 triggers, which required the two muons to have opposite charge and the pseudorapidity of the single muons, η^{μ}, to lie within $|\eta^{\mu}| < 1.6$ for one and $|\eta^{\mu}| < 1.4$ for the other trigger. Furthermore, the absolute difference in pseudorapidity between the two muons, $|\Delta\eta^{\mu}|$, had to be $|\Delta\eta^{\mu}| < 1.8$ at L1 in 2016. In 2017 for the first time an additional cut on the invariant mass of the muon pair as well as on the angular distance $\Delta\mathrm{R} \coloneqq \sqrt{(\Delta\eta)^2 + (\Delta\phi)^2}$ could be defined for the L1 trigger. In contrast to the L1 seed in 2016, where no selection on the single muon's p_{T} was made at Level-1, the L1 seed for the `HLT_Dimuon10_Upsilon_Barrel_Seagulls` trigger in 2017 required the single muons to have a minimum p_{T}^{μ} of 4.5 GeV and the pseudorapidity to fulfill $|\eta^{\mu}| < 2$. Additionally the invariant mass of the dimuons had to be in the range 7 to 18 GeV in 2017 and as in 2016 the two muons had to be charged oppositely.

After collecting the data of the decay leptons, the reconstruction of the $\chi_{\mathrm{b}}(1\mathrm{P}) \to \Upsilon(1\mathrm{S})\gamma$ candidates is made in three main steps:

1. The dimuon candidates are reconstructed by performing a kinematic

Table 2: Summary of the HLT selection criteria for 2016 and 2017. χ^2 prob. denotes the χ^2 probability of the dimuon vertex fit.

	2016	2017
	HLT_Dimuon8_Upsilon_Barrel	HLT_Dimuon10_Upsilon_Barrel_Seagulls
$p_{\mathrm{T}}^{\mu\mu} >$	7.9 GeV	9.9 GeV
$\lvert y^{\mu\mu}\rvert <$	1.25	1.25
$\lvert \eta^{\mu}\rvert <$	2.5	2.5
$m^{\mu\mu} >$	8.5 GeV	8.5 GeV
$m^{\mu\mu} <$	11.5 GeV	11.5 GeV
χ^2 prob. $>$	0.5%	0.5%
Only seagulls	No	Yes

vertex fit (KVF) [59] with two muons with opposite sign and then selecting the obtained dimuons that fulfill the dimuon selections in Table 2.

2. The photons are reconstructed from the electron-positron pairs originating from converted photons.

3. To obtain the $\chi_{\mathrm{b}}(1\mathrm{P})$ candidates from the dimuon and photon candidates a KVF with the following constraints is performed:

   - The muon and electron masses are bound to their physical masses.
   - The mass of the dimuon is constrained to the nominal mass of the $\Upsilon(1\mathrm{S})$.
   - The mass of the electron-positron pair is constrained to zero.
   - The two electrons are supposed to have a common vertex.
   - The two muon and the photon candidates are constrained to have a common vertex.

The mass distribution of the $\chi_{\mathrm{b}}(1\mathrm{P})$ candidates obtained from the KVF in step 3 is used for the $\chi_{\mathrm{b}}(1\mathrm{P})$ mass fits and is in the following denoted as m^{χ}. In the same manner the transverse momentum and rapidity from the KVF are referred to as p_{T}^{χ} and y^{χ}.

During the reconstruction also random $\chi_{\mathrm{b}}(1\mathrm{P})$ candidates are produced. This combinatorial background mainly consists of either $\Upsilon(1\mathrm{S})$ candidates combined with a random photon or totally random $\mu^+\mu^-\gamma$ combinations. For the analysis the following selections were applied to reduce the background and obtain a better separation between the $\chi_{\mathrm{b1}}(1\mathrm{P})$ and $\chi_{\mathrm{b2}}(1\mathrm{P})$ signal peaks:

- To reduce the bulk of the totally random $\mu^+\mu^-\gamma$ combinations the mass of the dimuon candidates is required to be in the $\pm 3\sigma$ region (where σ denotes the standard deviation) around the $\Upsilon(1S)$ mean value, μ. The values for the mean and the standard deviation of the $\Upsilon(1S)$ are obtained from a fit to the invariant dimuon mass distribution of the χ_b candidates. For the fit the shape of the $\Upsilon(1S)$ is modeled by the sum of two Crystal Ball (CB) functions, with the same mean but different widths and with a tail on the low and the high side. The $\Upsilon(2S)$ and $\Upsilon(3S)$ signal peaks are each described by one CB function with the tail on the low side and with their means fixed to the mean of the $\Upsilon(1S)$, scaled over the world average ratio of the mass [39], m_{PDG}, of the $\Upsilon(nS)$:

$$\mu[\Upsilon(2S,3S)] = \frac{m_{\mathrm{PDG}}[\Upsilon(2S,3S)]}{m_{\mathrm{PDG}}[\Upsilon(1S)]} \cdot \mu[\Upsilon(1S)].$$

  The parameter N which describes the tail of the CB function is fixed to $N = 3$ for all three $\Upsilon(nS)$ signal peaks on the low side, and to $N = 2$ on the high side of the $\Upsilon(1S)$. The other tail parameter α is left free for all states. The background is modeled by an exponential function. The results of the fits and the corresponding pull distributions are shown in Fig. 17 for 2016 and 2017. The same selection range was obtained for 2016 and 2017: $9.22 < p_{\mathrm{T}}^{\mu\mu} < 9.68\,\mathrm{GeV}$.

- The χ^2 probability of the $\chi_b(1P)$ KVF has to be greater than 1%.

- The masses of the $\chi_b(1P)$ candidates have to be in the range $9.70 < m^{\chi} < 10.15\,\mathrm{GeV}$.

- The distance in z direction between the dimuon vertex and the photon vertex, d_z, has to be below 5 mm.

- The pseudorapidity of the photon is required to fulfill $|\eta^{\gamma}| < 1.2$ to obtain the best possible resolution and thus separation between the $\chi_{b1}(1P)$ and $\chi_{b2}(1P)$ signals.

- The transverse momenta of the photons must have $p_{\mathrm{T}}^{\gamma} > 0.4\,\mathrm{GeV}$.

- The absolute rapidity of the muon pairs has to be within $|y^{\mu\mu}| < 1.2$.

- The single muons of 2016 are required to satisfy:

$$p_{\mathrm{T}}^{\mu} > \begin{cases} 3.5\,\mathrm{GeV} & \text{if} \quad 0 < |\eta^{\mu}| < 1.2 \\ [3.5 - 2.5 \cdot (|\eta^{\mu}| - 1.2)]\ \mathrm{GeV} & \text{if} \quad 1.2 < |\eta^{\mu}| < 1.6 \end{cases},$$

  to lie within a region with high acceptance and reconstruction efficiency. In 2017 the L1 trigger required a minimum p_{T} of the muons of

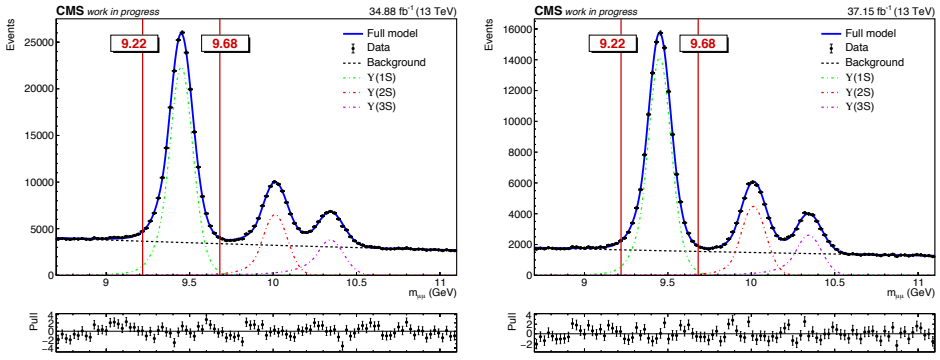

(a) 2016 (b) 2017

Figure 17: Result of the dimuon mass fit for 2016 (a) and 2017 (b). The fit is used to estimate the $\pm 3\sigma$ mass region for the selection of $\Upsilon(1S)$ events, indicated by the vertical red lines. The background is described by an exponential function, the $\Upsilon(1S)$ signal peak by two overlayed Crystal Ball functions and the $\Upsilon(2S)$ and $\Upsilon(3S)$ signal by a single Crystal Ball function.

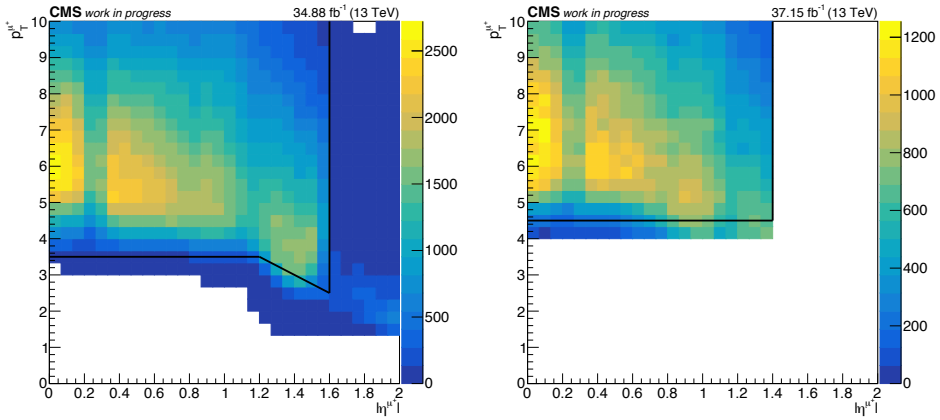

(a) 2016 (b) 2017

Figure 18: The p_{T}^{μ} over $|\eta^{\mu}|$ distributions of the positively charged muons for the full data sample for 2016 (left) and 2017 (right). The straight black lines show the single muon selections for this analysis. Muons with $|\eta^{\mu}| < 1.4$ were already selected at the processing step for 2017 data.

4.5 GeV. Additionally only muons with a pseudorapidity of $|\eta^{\mu}| < 1.4$ have been taken into account in this analysis. In Fig. 18 the p_{T}^{μ} over $|\eta^{\mu}|$ distribution and the applied single muon selections for 2016 and 2017 are shown for the positively charged muons.

To be able to exclude some relative polarization scenarios, simulated samples with different polarizations were produced for the $\chi_b(1P)$. As only the ratio of the χ_{b2} over the χ_{b1} events as function of $\cos\vartheta^{HX}$ are investigated, detector and reconstruction effects are assumed to be negligible. Thus, instead of the official CMS MC samples which fully simulate the detector and the reconstruction process, a faster, but for this analysis, in which detection and reconstruction effects are assumed to be negligible, adequate, simulation is used, which is referred to as fast MC in the following. The samples were produced within the following kinematic ranges:

- $0 < p_T^{\chi} < 60\,\text{GeV}$,
- $0 < |y^{\chi}| < 2$.

The $\chi_b(1P)$ is generated flat in rapidity and following the p_T/M distribution from Ref. [60]:

$$h\left(p_T/M\right) = \frac{p_T}{M} \cdot \left(1 + \frac{1}{\beta - 2} \cdot \frac{(p_T/M)^2}{\gamma}\right)^{-\beta}, \tag{5.1}$$

where M is the mass and β and γ are parameters which are determined from a fit to data [60]. The parameter γ has the meaning of the squared average of (p_T/M) and defines the function in the low p_T turn on region. The average world values are used for the masses [39]. The widths of the resonances are not taken into account since the width of the $\Upsilon(1S)$ meson is very narrow and for the $\chi_{b1}(1P)$ states no measurements exist. The angular distribution of the muons from the $\chi_b(1P)$ decay is generated for several extreme polarization scenarios in the helicity frame following the calculations in Ref. [49]. The photon properties are calculated obeying all conservation laws of the $\chi_b(1P) \to \Upsilon(1S)\gamma$ decay. After generation, the same selections as on data are applied on the fast MC samples.

5.3 Methods for yield extraction

The total data sample contains not only the interesting $\chi_{b1}(1P)$ and $\chi_{b2}(1P)$ events but also, even after applying all the selections introduced in Section 5.2, undesired background events. The signal is separated from the background in two ways:

1. The data sample is divided in several bins of $|\cos\vartheta^{HX}|$ and for each subsample a $\chi_b(1P)$ mass fit is performed. From the fits the number of $\chi_{b1}(1P)$ and $\chi_{b2}(1P)$ events is obtained for each bin. The $N^{\chi_{b2}}/N^{\chi_{b1}}$ ratio is then determined from the extracted yields as a function of $|\cos\vartheta^{HX}|$.

2. The second method uses the so called sPlot technique [61], which is a statistical tool to unfold the contributions of different sources in a data sample, keeping track of the statistical uncertainties. For the sPlot method two types of variables are defined:

   i) *Discriminating variables*: A set of variables for which the distributions of all sources of particles are known. In this analysis this is the m^{χ} distribution, including the $\chi_{b1}(1P)$ and $\chi_{b2}(1P)$ signal and background.

   ii) *Control variables*: A set of variables for which the distributions of the individual sources are unknown but can be obtained from the distributions of the discriminating variables. In this analysis the $\cos\vartheta^{HX}$ distribution is the control variable whereof the contributions of the $\chi_{b1}(1P)$ and $\chi_{b2}(1P)$ are extracted.

   To obtain the yields of the different sources a likelihood fit of the m^{χ} distribution is performed. For each event a weight that reflects how likely it is that the candidate is part of the background, part of the $\chi_{b1}(1P)$ signal or part of the $\chi_{b2}(1P)$ signal, is determined. The weights are used to get the $\cos\vartheta^{HX}$ distributions for the $\chi_{b1}(1P)$ as well as for the $\chi_{b2}(1P)$ events separately, and consequently their ratio can be obtained.

   The essential requirement for the sPlot technique is that the control variable is uncorrelated with the set of discriminating variable. Because the $\cos\vartheta^{HX}$ distribution is not fully uncorrelated from the m^{χ} distribution, the $\chi_{b2}(1P)/\chi_{b1}(1P)$ ratios are also obtained using the first method which performs $\cos\vartheta^{HX}$ binned $\chi_{b}(1P)$ mass fits.

The $|\cos\vartheta^{HX}|$ bins were chosen in a way that there are enough events for the fit of each subsample:

- 2016: {0,0.11,0.22,0.33,0.44,0.55,0.862},
- 2017: {0,0.11,0.22,0.33,0.44,0.824}.

For 2017 there is one bin less than for 2016 data in the upper $|\cos\vartheta^{HX}|$ region. This is necessary because of a lack of data in that region for 2017 which probably is due to the tighter selection of the single muons. Also the upper border for the last bin, which is determined by the last data point of the $\cos\vartheta^{HX}$ variable, is for 2017 smaller than for 2016. It is presumed that this effect can also be explained with the single muon selection used for the 2017 data sample.

5.4 Fit model

A fit to the mass distribution of the $\chi_{\mathrm{b}}(1\mathrm{P})$ candidates is performed to extract the $\chi_{\mathrm{b}1}(1\mathrm{P})$ and $\chi_{\mathrm{b}2}(1\mathrm{P})$ yields. The shape of the mass distribution is described by three probability density functions (PDFs): one for the background, one for the $\chi_{\mathrm{b}1}(1\mathrm{P})$ signal and one for the $\chi_{\mathrm{b}2}(1\mathrm{P})$ signal. The $J = 0$ state of the $\chi_{\mathrm{b}J}(1\mathrm{P})$ spin triplet has a branching in the radiative $\chi_{\mathrm{b}J}(1\mathrm{P}) \to \Upsilon(1\mathrm{S})\gamma$ decay of 2%, which is small compared to a value of 35% and 19% of the $J = 1$ and $J = 2$ state, respectively [39]. This causes a negligibly small yield for the $\chi_{\mathrm{b}0}(1\mathrm{P})$ state, which hence is not considered in the model describing the m^{χ} distribution.

A common choice for the description of signal peaks in high-energy physics is the CB function. The CB function has a Gaussian core, defined by the mean μ and the width σ, and a power-law tail for reflecting energy losses for example through final state radiation. The power-law tail is defined by the exponent N and a parameter α which describes the transition between the tail and the Gaussian core. Recent studies of the χ_{b} system at CMS [52] have shown that the signal shapes of the χ_{b} mass distributions also have a tail on the high mass side. Therefore a double-sided CB (DSCB) function, with a tail on the high and low mass side is used for the description of the signal peaks. The DSCB is defined as follows:

$$f_{\mathrm{DSCB}}(x) = \begin{cases} \exp\left(-\frac{x^2}{2}\right) & \text{if } -\alpha_{\mathrm{L}} < x < \alpha_{\mathrm{H}} \\ \exp\left(-\frac{\alpha_{\mathrm{L}}^2}{2}\right)\left[1 - \frac{\alpha_{\mathrm{L}}^2}{N_{\mathrm{L}}} - \frac{\alpha_{\mathrm{L}}}{N_{\mathrm{L}}}x\right]^{-N_{\mathrm{L}}} & \text{if } x < -\alpha_{\mathrm{L}} \\ \exp\left(-\frac{\alpha_{\mathrm{H}}^2}{2}\right)\left[1 - \frac{\alpha_{\mathrm{H}}^2}{N_{\mathrm{H}}} + \frac{\alpha_{\mathrm{H}}}{N_{\mathrm{H}}}x\right]^{-N_{\mathrm{H}}} & \text{if } x > \alpha_{\mathrm{H}} \end{cases}, \tag{5.2}$$

where $x = (m^{\chi} - \mu)/\sigma$ and N_{L}, α_{L}, N_{H} and α_{H} are the tail parameters for the tail on the low and high mass side, respectively. The change of the shape of the DSCB with a slight variation of the different parameters is shown in Fig. 19. The background is described by a second-order Chebychev polynomial with two free parameters c_0 and c_1:

$$f_{\mathrm{BG}}(x) = 1 + c_0 \cdot x + c_1 \cdot (2x^2 - 1). \tag{5.3}$$

The full model that is used for fitting the invariant mass distribution of the $\chi_{\mathrm{b}}(1\mathrm{P})$ candidates is composed of a DSCB function for the $\chi_{\mathrm{b}1}(1\mathrm{P})$ as well as for the $\chi_{\mathrm{b}2}(1\mathrm{P})$ signal and the background PDF:

$$f(m^{\chi}) = N^{\chi_{\mathrm{b}1}} \cdot f_{\mathrm{DSCB}}^{\chi_{\mathrm{b}1}} + N^{\chi_{\mathrm{b}2}} \cdot f_{\mathrm{DSCB}}^{\chi_{\mathrm{b}2}} + N^{\mathrm{bkg}} \cdot f_{\mathrm{BG}}, \tag{5.4}$$

where the parameters $N^{\chi_{\mathrm{b}1}}$, $N^{\chi_{\mathrm{b}2}}$ and N^{bkg} are the total numbers of $\chi_{\mathrm{b}1}(1\mathrm{P})$, $\chi_{\mathrm{b}2}(1\mathrm{P})$ and background candidates respectively and are responsible for the scaling of the individual PDFs.

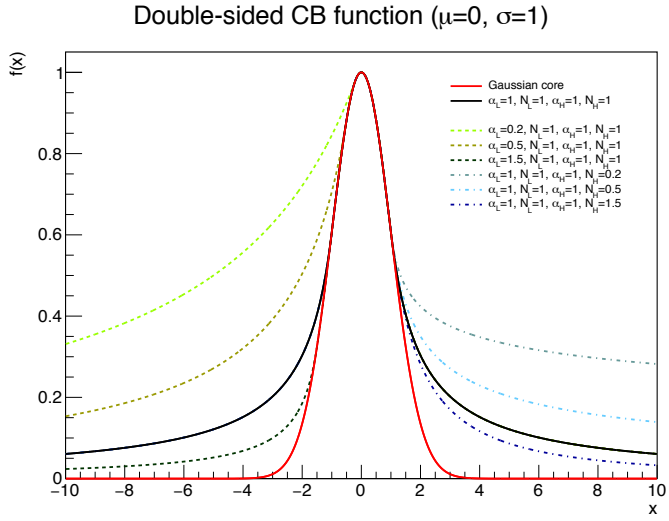

Figure 19: The shape of the double-sided CB function for different values for the parameters N_{L}, N_{H}, α_{L} and α_{H}. The left tail shows variations of α and the right tail variations of N. The Gaussian core with $\mu = 0$ and $\sigma = 1$ is plotted in red.

Because of a relatively small data sample a reduction of the number of free parameters is necessary. Especially for the mass fits performed in several $\cos\vartheta^{\mathrm{HX}}$ bins this is unavoidable because the number of events is further reduced by a factor of the size of the number of bins. Since the tail parameters, α and N are strongly correlated, the parameters N_{L} and N_{H} were fixed to $N_{\mathrm{L}} = 2.5$ and $N_{\mathrm{H}} = 2$ in this analysis. As was shown in Ref. [52] with MC samples, the parameters N_{L}, N_{H}, α_{L} and α_{H} of the $\chi_{\mathrm{b}2}(1\mathrm{P})$ peak can be assumed to be the same as for the $\chi_{\mathrm{b}1}(1\mathrm{P})$ peak. Thus, the parameters N_{L}, N_{H}, α_{L} and α_{H} describing the $\chi_{\mathrm{b}2}(1\mathrm{P})$ peak are set to be the same as the corresponding parameters of the $\chi_{\mathrm{b}1}(1\mathrm{P})$ signal model. The mean of the Gaussian core of the $\chi_{\mathrm{b}2}(1\mathrm{P})$ is also tied to the mean of the $\chi_{\mathrm{b}1}(1\mathrm{P})$ signal peak, using the so called photon-energy scale (PES). The PES takes into account that the reconstructed photon energy is affected by processes such as multiple scattering or radiation produced by the deceleration of charged particles and thus can differ from the true value. Since the natural widths of the $\chi_{\mathrm{b}1}(1\mathrm{P})$ and $\chi_{\mathrm{b}2}(1\mathrm{P})$ are assumed to be negligible, the resolution of the signal resonance is given by the energy of the $\chi_{\mathrm{b}1}(1\mathrm{P})$ and $\chi_{\mathrm{b}2}(1\mathrm{P})$ which also allows connecting the width of the $\chi_{\mathrm{b}2}(1\mathrm{P})$ signal to the one of the $\chi_{\mathrm{b}1}(1\mathrm{P})$. The mean and width of the $\chi_{\mathrm{b}2}(1\mathrm{P})$ peak are connected to the $\chi_{\mathrm{b}1}(1\mathrm{P})$ values as follows:

$$\begin{aligned} \mu^{\chi_{\mathrm{b}2}} &= f_{\mathrm{Q}} \cdot \left(\mu^{\chi_{\mathrm{b}1}} - m_{\mathrm{PDG}}^{\Upsilon(1\mathrm{S})}\right) + m_{\mathrm{PDG}}^{\Upsilon(1\mathrm{S})}, \\ \sigma^{\chi_{\mathrm{b}2}} &= f_{\mathrm{Q}} \cdot \sigma^{\chi_{\mathrm{b}1}}, \end{aligned} \tag{5.5}$$

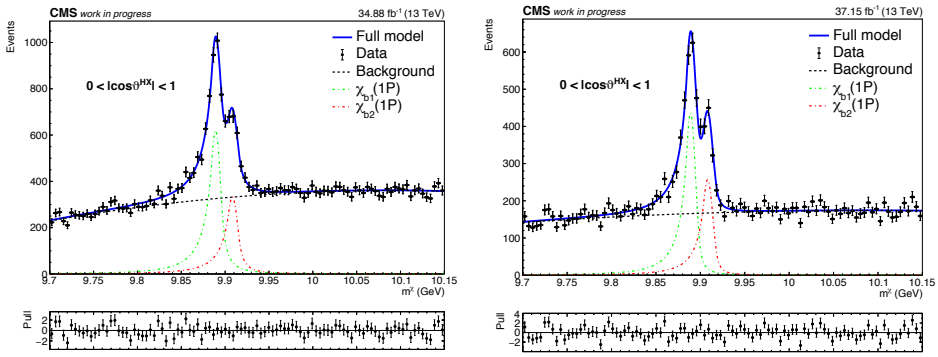

(a) 2016 (b) 2017

Figure 20: The invariant mass distribution of the $\chi_{\mathrm{b}}(1\mathrm{P})$ candidates fit with the model given in Eq. 5.4, for the range $|\cos\vartheta^{\mathrm{HX}}| < 1$, for 2016 (left) and 2017 (right) data. The individual fit components and the pull distribution are also shown.

where the factor f_{Q} is defined as

$$f_{\mathrm{Q}} = \frac{m^{\chi_{\mathrm{b}2}}_{\mathrm{PDG}} - m^{\Upsilon(1\mathrm{S})}_{\mathrm{PDG}}}{m^{\chi_{\mathrm{b}1}}_{\mathrm{PDG}} - m^{\Upsilon(1\mathrm{S})}_{\mathrm{PDG}}},$$

using the world average masses, m_{PDG}, as given in Ref. [39]. In total nine parameters are used for the m^{χ} fit:

- Four parameters describing the signal shapes: μ, σ, α_{L}, α_{H}.
- Two parameters modeling the background shape: c_0, c_1.
- And most importantly three normalization parameters giving the number of events: $N^{\chi_{\mathrm{b}1}}$, $N^{\chi_{\mathrm{b}2}}$ and N^{bkg}.

The mass distributions of the $\chi_{\mathrm{b}1}(1\mathrm{P})$ events in the full $\cos\vartheta^{\mathrm{HX}}$ range and the corresponding fit results, which are used for the sPlot method, are displayed in Fig. 20. Figures 21 and 22 show the mass distributions and their fits in different bins of $|\cos\vartheta^{\mathrm{HX}}|$. As can be seen from the pull distributions, the model describes the data reasonably well for the integrated as well as for the binned fits. The number of $\chi_{\mathrm{b}1}(1\mathrm{P})$ and $\chi_{\mathrm{b}2}(1\mathrm{P})$ events obtained from the fits are listed in Table 3 and plotted in Fig. 23 as a function of $|\cos\vartheta^{\mathrm{HX}}|$. Within the uncertainties, which are also considering fit correlations, the $N^{\chi_{\mathrm{b}2}}/N^{\chi_{\mathrm{b}1}}$ ratio is flat over the whole $|\cos\vartheta^{\mathrm{HX}}|$ range and the yields obtained with the different methods are comparable. In Fig. 24 the widths of the signal peaks, σ, and the parameter α_{L} of the DSCB function

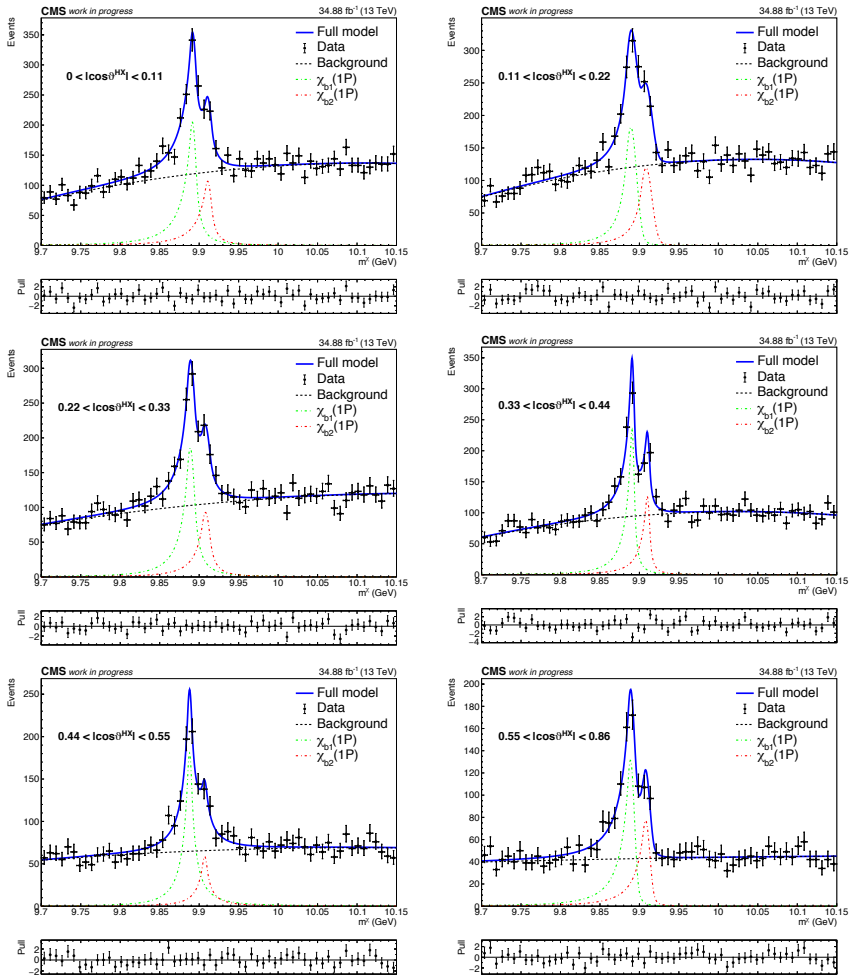

Figure 21: The invariant mass distribution of the $\chi_{\mathrm{b1}}(1\mathrm{P})$ events fit with the model given in Eq. 5.4 and for the $|\cos\vartheta^{\mathrm{HX}}|$ ranges indicated in the plots, for 2016 data. The individual fit components and the pull distributions are also shown.

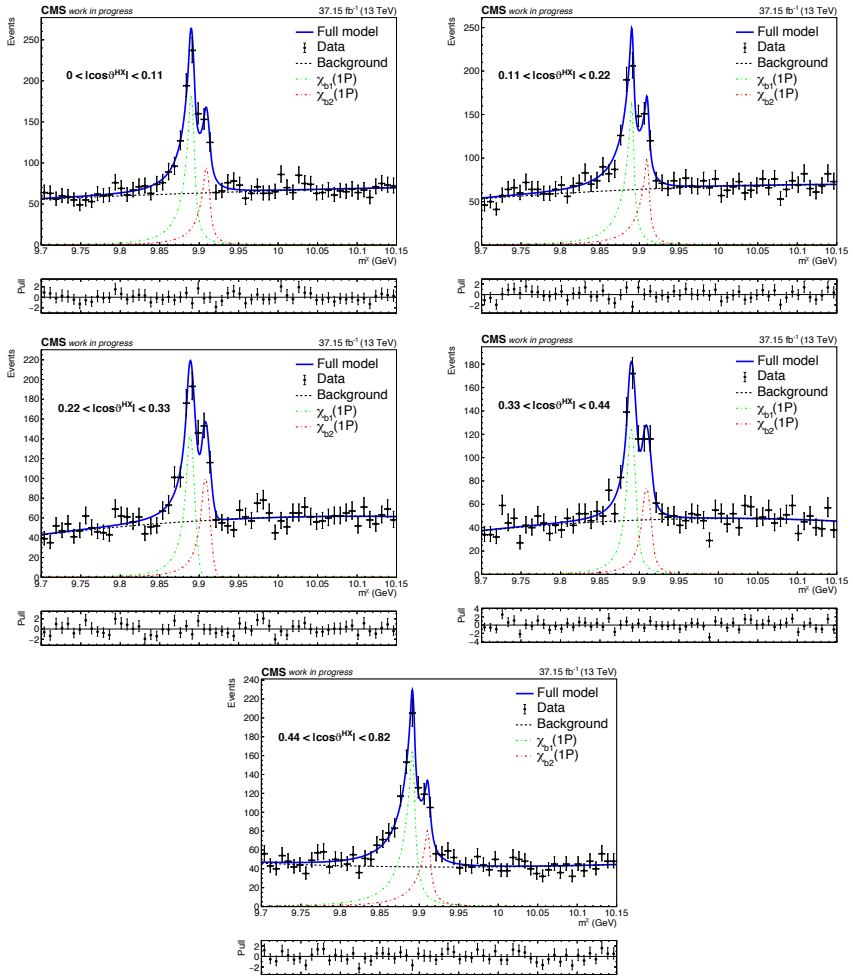

Figure 22: The invariant mass distribution of the $\chi_{\mathrm{b1}}(1\mathrm{P})$ events fit with the model given in Eq. 5.4 and for the $|\cos\vartheta^{\mathrm{HX}}|$ ranges indicated in the plots, for 2017 data. The individual fit components and the pull distributions are also shown.

Table 3: The number of χ_{b1} and χ_{b2} events and the relative number $N^{\chi_{b2}}/N^{\chi_{b1}}$ and their uncertainty obtained from the fits for 2016 (top) and 2017 (bottom). The uncertainties of the $N^{\chi_{b2}}/N^{\chi_{b1}}$ ratio also consider fit correlations.

	2016		
	$N^{\chi_{b1}}$	$N^{\chi_{b2}}$	$N^{\chi_{b2}}/N^{\chi_{b1}}$
$0 < \lvert\cos\vartheta^{HX}\rvert < 0.11$	753 ± 101	410 ± 72	0.545 ± 0.141
$0.11 < \lvert\cos\vartheta^{HX}\rvert < 0.22$	608 ± 61	418 ± 60	0.687 ± 0.132
$0.22 < \lvert\cos\vartheta^{HX}\rvert < 0.33$	669 ± 88	350 ± 61	0.523 ± 0.127
$0.33 < \lvert\cos\vartheta^{HX}\rvert < 0.44$	545 ± 50	308 ± 42	0.566 ± 0.094
$0.44 < \lvert\cos\vartheta^{HX}\rvert < 0.55$	570 ± 85	194 ± 47	0.340 ± 0.114
$0.55 < \lvert\cos\vartheta^{HX}\rvert < 0.86$	422 ± 43	259 ± 39	0.615 ± 0.122
$0 < \lvert\cos\vartheta^{HX}\rvert < 1$	3517 ± 163	1974 ± 126	0.561 ± 0.051

	2017		
	$N^{\chi_{b1}}$	$N^{\chi_{b2}}$	$N^{\chi_{b2}}/N^{\chi_{b1}}$
$0 < \lvert\cos\vartheta^{HX}\rvert < 0.11$	525 ± 60	286 ± 46	0.545 ± 0.124
$0.11 < \lvert\cos\vartheta^{HX}\rvert < 0.22$	466 ± 55	300 ± 48	0.645 ± 0.143
$0.22 < \lvert\cos\vartheta^{HX}\rvert < 0.33$	384 ± 35	279 ± 37	0.725 ± 0.125
$0.33 < \lvert\cos\vartheta^{HX}\rvert < 0.44$	348 ± 41	216 ± 33	0.621 ± 0.128
$0.44 < \lvert\cos\vartheta^{HX}\rvert < 0.82$	553 ± 64	281 ± 45	0.508 ± 0.117
$0 < \lvert\cos\vartheta^{HX}\rvert < 1$	2151 ± 102	1324 ± 88	0.616 ± 0.055

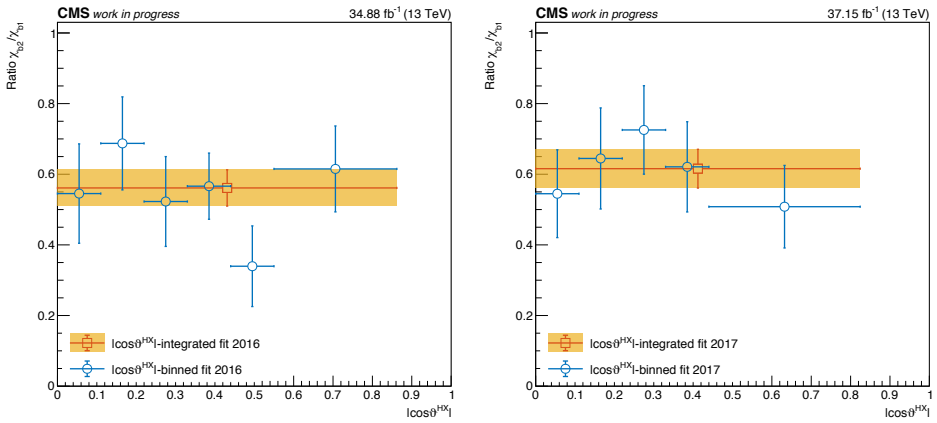

(a) 2016 (b) 2017

Figure 23: The $N^{\chi_{b2}}/N^{\chi_{b1}}$ ratio obtained from the fits of the $|\cos\vartheta^{HX}|$-binned subsamples (blue) and from the m^{χ} fit over the full $\cos\vartheta^{HX}$ range (yellow area) for 2016 (a) and 2017 (b). In the uncertainties fit correlations are considered.

are shown as a function of $\cos\vartheta^{HX}$ for 2016 and 2017. The strong variation of the width of the $\chi_{b1}(1P)$ signal can be explained by changes in the shape of the DSCB between different bins. The DSCB turned out to be very sensitive to the start values of the parameters of the fit, which had to be chosen individually for each bin to obtain acceptable results. From the fit results in Figs. 21 and 22 it can be seen that even if the shape of the DSCB functions vary for each bin, the total shape is still well described, which shows the strong correlation between the parameters of the DSCB function. Looking at the similar change in the shape of the width of the Gaussian core and the tail parameter α_L in Fig. 24 as a function of $|\cos\vartheta^{HX}|$, further illustrates the correlation between the parameters of the DSCB function. As an alternative to the DSCB a combination of a Gaussian core and two exponential functions on each side, as proposed in Ref. [62], could be tried in future studies, since this approach would have one parameter less for each tail.

The description of the background seems to work well with second-order Chebychev polynomials. Figure 25 shows the variation of the background parameter c_0 (the linear part in Eq. 5.3) as a function of $\cos\vartheta^{HX}$. The change of c_0 indicates that the change of the background in dependence of $\cos\vartheta^{HX}$ is more relevant for 2016 data. The difference in the behavior of the background can possibly be explained by the upgrade of the inner tracker between the two data taking periods, which probably lead to a better photon identification and hence less background events.

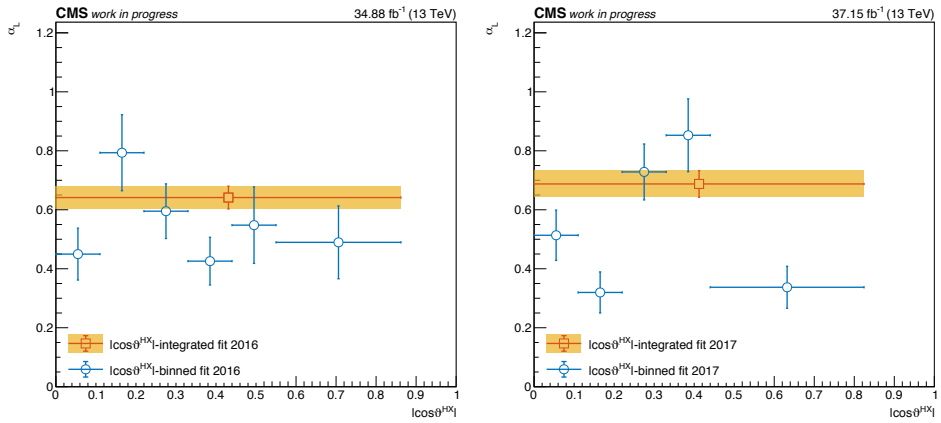

(a) Parameter α_{L} 2016

(b) Parameter α_{L} 2017

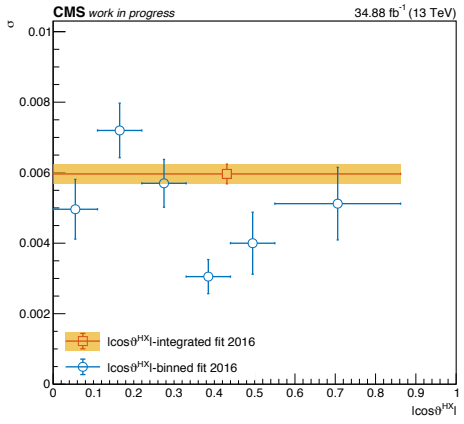

(c) Width σ 2016

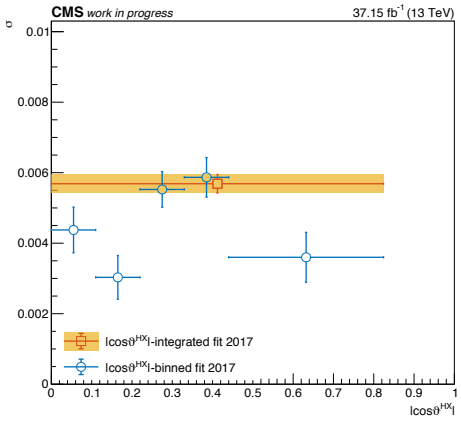

(d) Width σ 2017

Figure 24: The tail parameter α_{L} of the DSCB function as a function of $|\cos\vartheta^{\mathrm{HX}}|$ for 2016 (a) and 2017 (b). The width of the $\chi_{\mathrm{b1}}(1\mathrm{P})$ signal peak obtained in the fits as function of $|\cos\vartheta^{\mathrm{HX}}|$ for 2016 (c) and 2017 (d). The width of the $\chi_{\mathrm{b2}}(1\mathrm{P})$ signal is related to the $\chi_{\mathrm{b1}}(1\mathrm{P})$ width through PES. The yellow area represents the value obtained from the m^{χ} fit over the full $|\cos\vartheta^{\mathrm{HX}}|$ range.

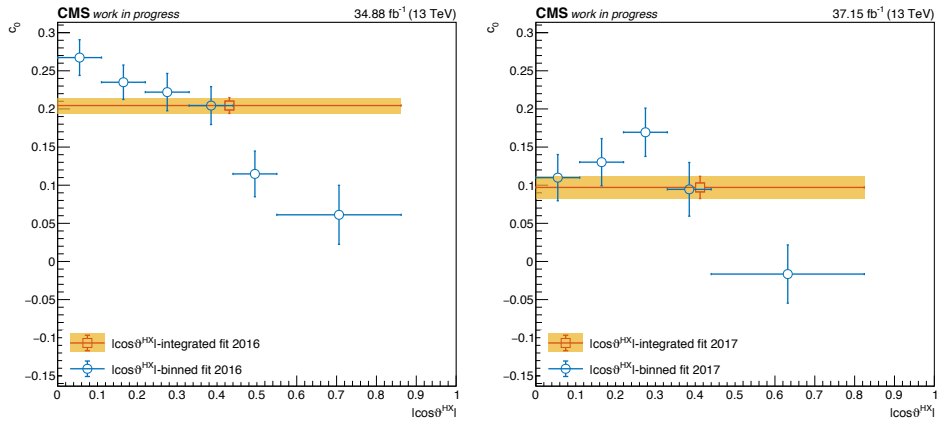

(a) 2016 (b) 2017

Figure 25: The parameter c_0 of the background function given in Eq. 5.3, which describes the linear part, as a function of $|\cos\vartheta^{\mathrm{HX}}|$ for 2016 and 2017. The yellow area represents the value obtained from the m^{χ} fit over the full $|\cos\vartheta^{\mathrm{HX}}|$ range.

5.5 Systematic uncertainties

Systematic uncertainties coming from the detector acceptance, trigger, reconstruction and muon and photon efficiencies cancel largely in the ratio of $\chi_{\mathrm{b}2}(1\mathrm{P})$ over $\chi_{\mathrm{b}1}(1\mathrm{P})$ events. These effects mainly depend on the momentum of the detected particles, i.e. the decay products of the χ_{b}. In Fig. 26 the ratio of the p_{T} distributions of the photons and muons of the $\chi_{\mathrm{b}2}(1\mathrm{P})$ divided by the one of the $\chi_{\mathrm{b}1}(1\mathrm{P})$ candidates is shown. It can be seen that the ratio is, within the errors, flat and hence the differences of the photon and muon p_{T} of the $\chi_{\mathrm{b}1}(1\mathrm{P})$ and the $\chi_{\mathrm{b}2}(1\mathrm{P})$ candidates are small, which indicate that the mentioned effects should largely cancel in the ratio. Besides, a still ongoing study of relative $\chi_{\mathrm{c}2}/\chi_{\mathrm{c}1}$ polarizations, which uses similar analysis techniques, has shown the cancellation of efficiency effects in the ratio on fast MC samples. That the mass difference of the $\chi_{\mathrm{b}1}(1\mathrm{P})$ and the $\chi_{\mathrm{b}2}(1\mathrm{P})$ state, which is 19 MeV, is smaller than the $\chi_{\mathrm{c}1}(1\mathrm{P})$ and $\chi_{\mathrm{c}2}(1\mathrm{P})$ mass difference (45 MeV) suggests that the $\chi_{\mathrm{b}1}(1\mathrm{P})$ and $\chi_{\mathrm{b}2}(1\mathrm{P})$ candidates should be even more alike than the corresponding ones of the χ_{c} system. Therefore, only systematic uncertainties related to the mathematical model used for the fitting of the invariant mass distributions of the $\chi_{\mathrm{b}1}(1\mathrm{P})$ candidates are considered.

The systematic uncertainties from the extraction of the $\chi_{\mathrm{b}1}(1\mathrm{P})$ and $\chi_{\mathrm{b}2}(1\mathrm{P})$ yields are evaluated separately for the signal and the background model. Changing the signal model completely and still obtaining a good description of the data is almost impossible. Therefore, instead, the param-

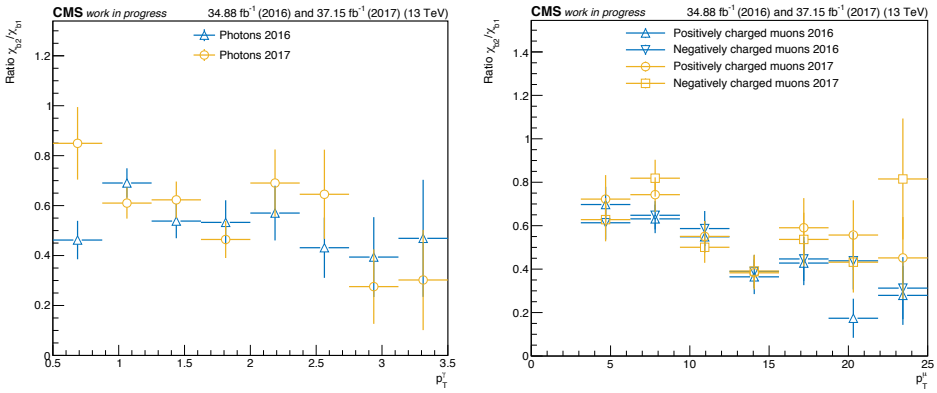

(a) Photons (b) Muons

Figure 26: Ratio of $\chi_{b2}(1P)$ over $\chi_{b1}(1P)$ events as a function of the p_T of the photons (a) and muons (b) for 2016 and 2017 data.

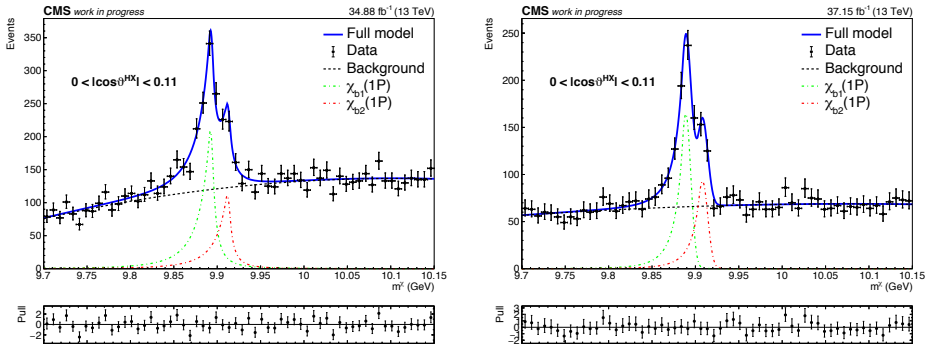

(a) 2016 (b) 2017

Figure 27: Examples for a fit result for the estimation of the systematic uncertainty from the signal model for 2016 (a) and 2017 (b). The parameters α_L,N_L, α_H and N_H have all been left free in this fit.

eters of the DSCB, N_L and N_H, that are fixed in the nominal fit are left free in an alternative fit. The systematic uncertainty due to the chosen signal shape is then obtained by the difference in the ratio of the number of events between the nominal and the alternative fit. An example for the fitresult obtained when leaving N_L and N_H free is shown in Fig. 27. As can be seen from the pull distribution the fit worked reasonably well.

To estimate the systematic uncertainty related to the chosen background model, the variation in the yield ratio between the nominal model and an

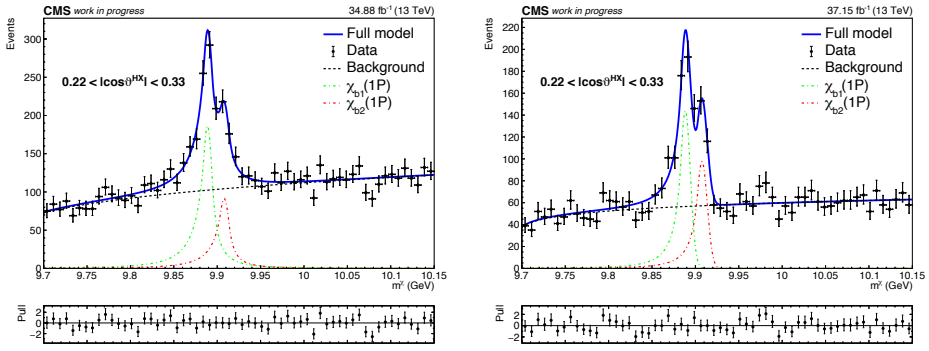

(a) 2016 (b) 2017

Figure 28: Examples for the fit results for the estimation of the systematic uncertainties from the background model for 2016 (a) and 2017 (b). The background is desribed by a power law given in Eq. 5.6.

alternative background model, a power law,

$$f_{\text{pow}}(x) = (x - x_0)^{\nu}, \tag{5.6}$$

with the free parameters x_0 and ν, is used. In Fig. 28 an example of the fit results with the alternative background description is shown for 2016 and 2017.

The background and signal systematic errors are added in quadrature to determine the total systematic uncertainty due to the extraction of the yields. The total relative systematic uncertainties are displayed in Fig. 29, together with the statistical uncertainties of the $\chi_{\text{b2}}(1\text{P})/\chi_{\text{b1}}(1\text{P})$ ratio. The statistical uncertainty is obtained from the $\chi_{\text{b1}}(1\text{P})$ and $\chi_{\text{b2}}(1\text{P})$ yields taking into account fit correlations. For the calculation of the total uncertainty the systematic and statistical uncertainty are added in quadrature for each bin.

For both years the statistical uncertainties are dominating over the systematic uncertainties. Further it can be said for both years that the statistical as well as the systematic uncertainties of the $N^{\chi_{\text{b2}}}/N^{\chi_{\text{b1}}}$ ratio have on average larger values for the method using $|\cos\vartheta^{\text{HX}}|$ binned subsamples. Each, the systematic and statistical uncertainties for 2017 are, aside from the bin with $0.22 < |\cos\vartheta^{\text{HX}}| < 0.33$ which has an conspicuous lower statistical and systematic uncertainty for the binned method, comparable over all $|\cos\vartheta^{\text{HX}}|$ bins and each method. That the bin in the range $0.22 < |\cos\vartheta^{\text{HX}}| < 0.33$ has a smaller systematic and statistical uncertainty for the method using subsamples indicates that for this $|\cos\vartheta^{\text{HX}}|$ subsample the fit is more stable than for the other bins. For the fits with 2016 data the uncertainties show

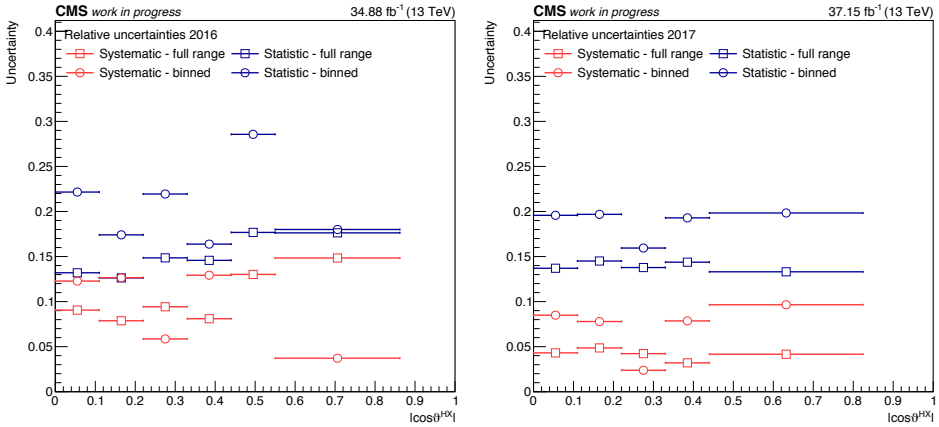

(a) 2016 (b) 2017

Figure 29: The relative systematic (red) and statistical (blue) uncertainties as a function of $|\cos\vartheta^{\mathrm{HX}}|$ for both methods for 2016 (a) and 2017 (b) data. The relative uncertainties of the method using data subsamples in bins of $|\cos\vartheta^{\mathrm{HX}}|$ are marked with a circle and the ones using the sPlot technique with squares. The statistical uncertainty also considers fit correlations. For the $0.44 < |\cos\vartheta^{\mathrm{HX}}| < 0.55$ bin, the systematic error of the binned fit method for 2016 data is not shown in the plot, it has a value of 0.64.

much more fluctuations than for 2017 data, especially the statistical uncertainty of the method that performs a fit for different $|\cos\vartheta^{\mathrm{HX}}|$ subsamples shows fluctuations which reach from a minimum of 0.06 to a maximum relative error of 0.64. Although the fits could be assumed to perform well when looking at the pull distributions in Fig. 21, this fluctuations indicate that the fitting procedure for the $|\cos\vartheta^{\mathrm{HX}}|$ binned subsamples has to be investigated in more detail for future studies, at least for 2016 data.

5.6 Results

The yields of the $\chi_{\mathrm{b}2}(1\mathrm{P})/\chi_{\mathrm{b}1}(1\mathrm{P})$ are obtained with two different methods described in Section 5.3. The results determined by performing a $\chi_{\mathrm{b}}(1\mathrm{P})$ mass fit for each $|\cos\vartheta^{\mathrm{HX}}|$-binned subsample are compared to the ones from using the sPlot technique, which extracts a weight for each event from one $\chi_{\mathrm{b}}(1\mathrm{P})$ mass fit over the full $\cos\vartheta^{\mathrm{HX}}$ range. Figures 30 and 31 show the $N^{\chi_{\mathrm{b}2}}/N^{\chi_{\mathrm{b}1}}$ yields as a function of $\cos\vartheta^{\mathrm{HX}}$ for the 2016 and 2017 data samples. Within the large uncertainties, the ratio shows no great dependence on $\cos\vartheta^{\mathrm{HX}}$. The large uncertainties, which are obtained as described in Section 5.5, are a consequence of the low total number of $\chi_{\mathrm{b}}(1\mathrm{P})$ events. The squared markers in the plot show the average $|\cos\vartheta^{\mathrm{HX}}|$ value for each

bin. It can be seen that for the last bin the dominating number of events has a $|\cos\vartheta^{\mathrm{HX}}|$ value close to the lower bin edge, whereas the averages of the other bins are central. With both methods comparable yields are determined within the uncertainties. It seems that the sPlot technique, which uses just one $\chi_{\mathrm{b}}(1\mathrm{P})$ mass fit for the whole $|\cos\vartheta^{\mathrm{HX}}| < 1$ range, is only influenced negligibly by a correlation of the discriminating variable, m^{χ}, and the control variable, $\cos\vartheta^{\mathrm{HX}}$. Therefore the sPlot technique should be applicable for obtaining the yields of the ratio of $\chi_{\mathrm{b}2}(1\mathrm{P})$ over $\chi_{\mathrm{b}2}(1\mathrm{P})$ events as a function of $|\cos\vartheta^{\mathrm{HX}}|$. As shown in Section 5.5 the statistical as well as the systematic uncertainties of both methods, at least for 2017, are also consistent what is a strong hint that they are correctly calculated with the sPlot technique.

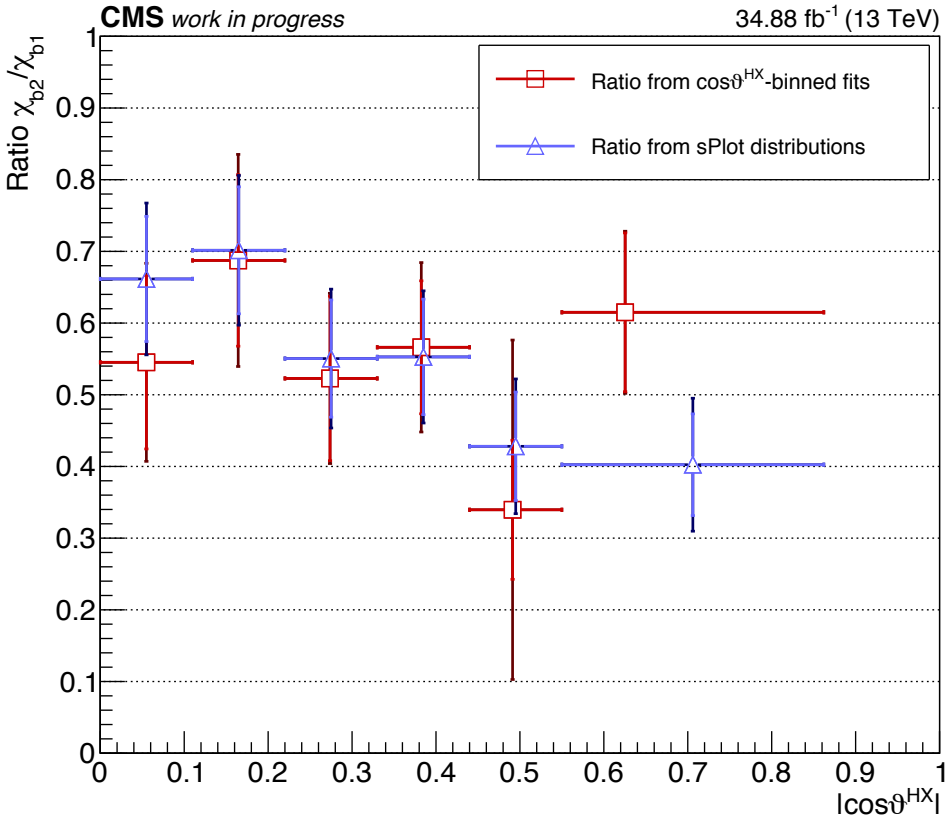

Figure 30: The $\chi_{b2}(1P)/\chi_{b1}(1P)$ as a function of $|\cos\vartheta^{HX}|$, once obtained with the sPlot technique (blue) and once with m^{χ} fits in $|\cos\vartheta^{HX}|$ bins (red), for 2016 data. The full error bars are showing the total uncertainties. The statistical uncertainty, which considers fit correlations, is shown separately in a lighter color. The triangles mark the middle of the bin, whereas the squares are placed at the average $|\cos\vartheta^{HX}|$ value for this bin including background events.

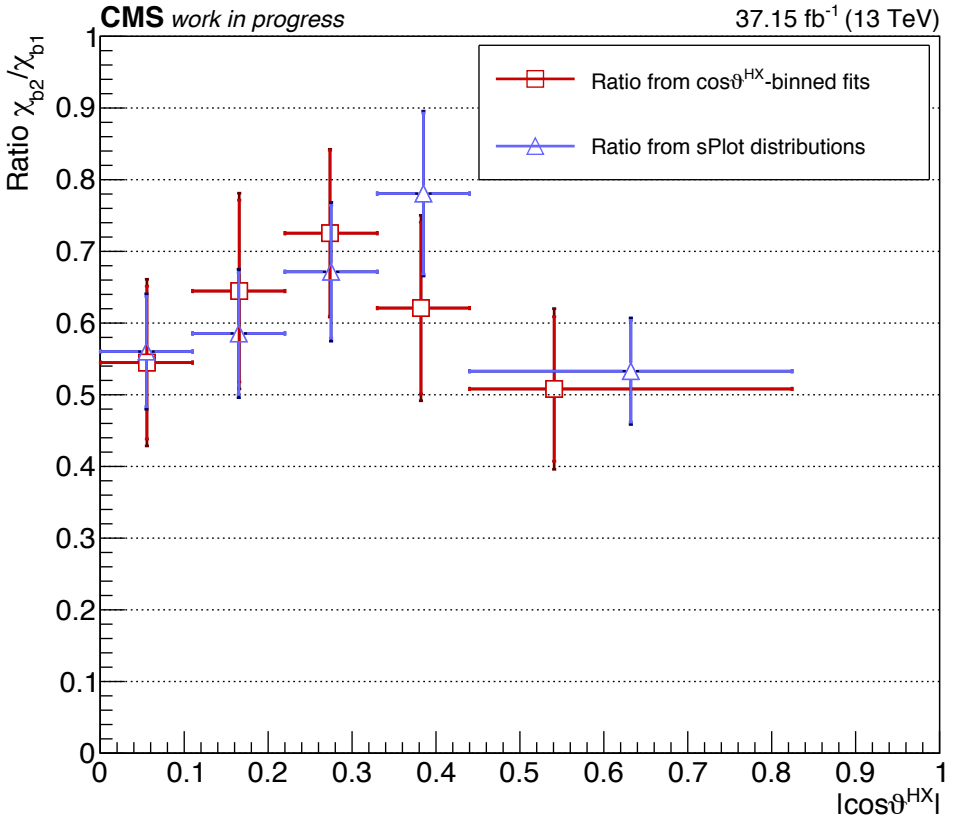

Figure 31: The $\chi_{b2}(1P)/\chi_{b1}(1P)$ event ratio as a function of $|\cos\vartheta^{HX}|$, once obtained with the sPlot technique (blue) and once with m^{χ} fits in $|\cos\vartheta^{HX}|$ bins (red), for 2017 data. The full error bars are showing the total uncertainties. The statistical uncertainty, which considers fit correlations, is shown separately in a lighter color. The triangles mark the middle of the bin, whereas the squares are placed at the average $|\cos\vartheta^{HX}|$ value for this bin including background events.

Chapter 6

Discussion of results

For discussing the obtained $\chi_{b2}(1P)/\chi_{b1}(1P)$ ratios as a function of $\cos\vartheta^{HX}$, fast MC samples were produced for the $\chi_{b1}(1P)$ and the $\chi_{b2}(1P)$ states with different polarizations in the helicity frame. After applying the same selections as on data, the different scenarios have been determined from the produced $\cos\vartheta^{HX}$ distributions by dividing the $\cos\vartheta^{HX}$ distributions of the $\chi_{b2}(1P)$ over the ones of the $\chi_{b1}(1P)$ using the same $\cos\vartheta^{HX}$ bins as for data. When the ratio of a $\cos\vartheta$ distribution with the polarization parameter λ_ϑ^2 over one with the polarization λ_ϑ^1 is built, the obtained shape is defined by the difference of the two parameters, $\Delta\lambda_\vartheta = \lambda_\vartheta^2 - \lambda_\vartheta^1$ [63]. For the comparison the most extreme scenarios of λ_ϑ, which can be deduced from Fig. 13 for the $\chi_{b1}(1P)$ and the $\chi_{b2}(1P)$ when setting $\lambda_\varphi = \lambda_{\vartheta\varphi} = 0$, are chosen. The minimum obtainable value is $\Delta\lambda_\vartheta = -8/5$, in which case $\lambda_\vartheta^{\chi_{b1}(1P)} = 1$, which is the maximum possible positive polarization for the $\chi_{b1}(1P)$, and $\lambda_\vartheta^{\chi_{b2}(1P)} = -3/5$, which is the maximum negative polarization of the $\chi_{b2}(1P)$. The maximum $\Delta\lambda_\vartheta$ has a value of $4/3$, realized by combining the extreme λ_ϑ values $\lambda_\vartheta^{\chi_{b1}(1P)} = -1/3$ and $\lambda_\vartheta^{\chi_{b2}(1P)} = 1$. A value of $\Delta\lambda_\vartheta = 0$ is reached by the combination of the following pairs of λ_ϑ values: $(\lambda_\vartheta^{\chi_{b1}(1P)}, \lambda_\vartheta^{\chi_{b2}(1P)}) = \{(-1/3, -1/3), (1, 1), (0, 0)\}$. These combinations always give a flat ratio. In Figs. 32 and 33 the different simulated relative polarization scenarios are shown overlaid with the measured values, which have been obtained by performing a $\chi_b(1P)$ mass fit for each $\cos\vartheta^{HX}$ bin and using the sPlot technique, respectively. Since only the shape of the $\chi_{b2}(1P)/\chi_{b1}(1P)$ ratio is relevant for the comparison, the normalization of the fast MC ratio in the plots is made in a way to be best comparable to data. The distributions obtained using the sPlot technique, shown in Fig. 33, have a shape that goes down with $|\cos\vartheta^{HX}|$ for 2016 but for 2017 the opposite seems the case for all but the last bin. The differences between the two data samples are the different transverse momentum minima for the dimuon, which were 8 GeV in 2016 and 10 GeV in 2017 and the different single muon selection

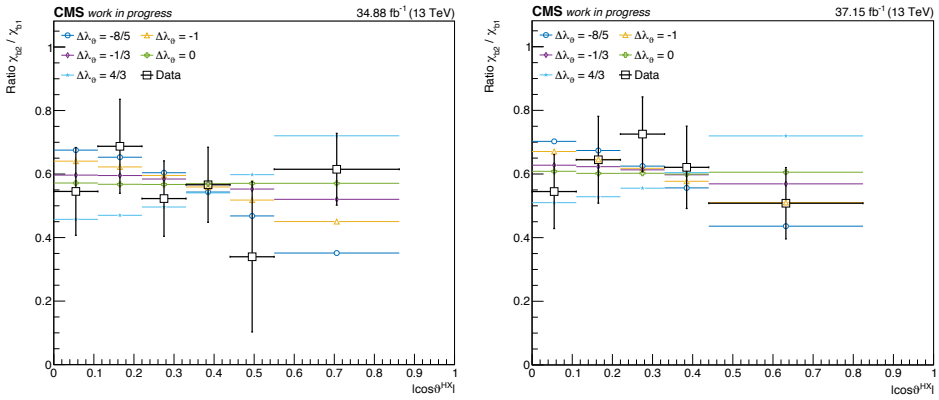

(a) 2016 (b) 2017

Figure 32: The measured shape of the relative $\chi_{b2}(1P)/\chi_{b1}(1P)$ polarization obtained using the method with $\cos\vartheta^{HX}$-binned fits compared to different relative polarization scenarios from fast MC samples. The error bars include the systematic and the statistical errors. The relative polarization scenarios from fast MC simulations are indicated in the plot with the parameter $\Delta\lambda_\vartheta$, which designates the difference of the polarization parameter λ_ϑ of the $\chi_{b2}(1P)$ and the $\chi_{b1}(1P)$.

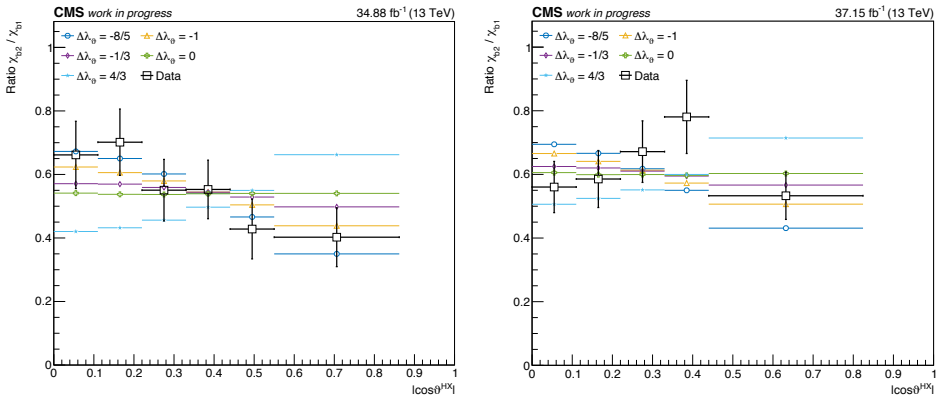

(a) 2016 (b) 2017

Figure 33: The measured shape of the relative $\chi_{b2}(1P)/\chi_{b1}(1P)$ polarization obtained using the sPlot technique compared to different relative polarization scenarios from fast MC samples. The error bars include the systematic and the statistical errors. The relative polarization scenarios from fast MC simulations are indicated in the plot with the parameter $\Delta\lambda_\vartheta$, which designates the difference of the polarization parameter λ_ϑ of the $\chi_{b2}(1P)$ and the $\chi_{b1}(1P)$.

criteria, which were stricter for 2017, where also only muon pairs that bend away from each other were allowed. If this possibly is an explanation has to be scrutinized with a much larger data sample which would allow to obtain these distributions additionally for different bins of transverse momentum. The trend for 2017 is also recognizable, at least for the first three bins, in Fig. 32(b), which is showing the $N^{\chi_{b2}}/N^{\chi_{b1}}$ event yields obtained from the m^{χ} fits using $\cos\vartheta^{\mathrm{HX}}$-binned subsamples. But having in mind the large uncertainties and the very different shapes, which suggest an possible underestimation of the systematical uncertainty, no clear trend of the shape can be identified. It was also tried to fit the measured ratios to the different shapes obtained from fast MC samples leaving the normalization a free parameter, but because of the large uncertainties no $\Delta\lambda_{\vartheta}$ scenario could be excluded with a reasonable significance in this way.

To get significant results a significantly larger data sample for reaching a better statistical precision would be necessary. It could be tried to combine the two datasets of 2016 and 2017 to obtain more meaningful shapes for the relative $\chi_{b2}(1P)/\chi_{b1}(1P)$ polarization.

Chapter 7

Conclusion and outlook

Polarization measurements of the P-wave states of quarkonium are important for proving theoretical predictions of QCD. This thesis investigated the $\chi_{\mathrm{b}}(1\mathrm{P})$ state of bottomonium. It was tried to measure the relative $\chi_{\mathrm{b}2}(1\mathrm{P})/\chi_{\mathrm{b}1}(1\mathrm{P})$ polarization using two different methods. Both methods rely on a stable fit of the $\chi_{\mathrm{b}}(1\mathrm{P})$ mass distribution, thus a suitable model for the description of the mass distribution is essential. The $\chi_{\mathrm{b}1}(1\mathrm{P})$ and $\chi_{\mathrm{b}2}(1\mathrm{P})$ signal resonances have been described with a DSCB function in this thesis and the background with a second-order Chebychev polynomial. Although the fits performed reasonably well, for the full $\cos\vartheta^{\mathrm{HX}}$ range as well as for the binned subsamples, it is concluded that a reconsideration of the fit model is needed, since the accurate description of the signal shapes of the $\chi_{\mathrm{b}1}(1\mathrm{P})$ and $\chi_{\mathrm{b}2}(1\mathrm{P})$ are crucial for both methods. The large uncertainties, which are mainly due to too little data for such a delicate analysis, made it even impossible to give at least a vague estimation of a trend of the shape of the relative $\chi_{\mathrm{b}2}(1\mathrm{P})/\chi_{\mathrm{b}1}(1\mathrm{P})$ polarization. Disregarding the lack of data it would be important to also obtain the relative polarization, aside from the helicity frame, in at least one additional frame, and also the φ distribution should be included in future studies with a larger data sample. For the application of the sPlot technique a study of the correlation between the $\chi_{\mathrm{b}}(1\mathrm{P})$ mass and the $\cos\vartheta$ distribution would be necessary. Another open question is if the acceptance and efficiency effects, which were here assumed to be negligible, really do not influence the shape of the $\chi_{\mathrm{b}2}(1\mathrm{P})/\chi_{\mathrm{b}1}(1\mathrm{P})$ ratio.

Although no relative $\chi_{\mathrm{b}2}(1\mathrm{P})/\chi_{\mathrm{b}1}(1\mathrm{P})$ polarization scenario could be excluded in this thesis, two methods to obtain the relative polarization have been analyzed in detail for future analyses. At the moment of writing the CMS detector has already recorded an integrated luminosity of nearly $50\,\mathrm{fb}^{-1}$ which is already more than in the data taking periods 2016 and 2017 [24]. Combining the data recorded in the years from 2015 to 2018 will lead to a data sample that should be appropriate for an analysis of the

polarization of the $\chi_b(1P)$. Such delicate polarization measurements of the P-wave states of quarkonium will only be possible in the future thanks to the enduring performance of the LHC, delivering more and more data.

Bibliography

[1] UA1 Collaboration. "Experimental observation of isolated large transverse energy electrons with associated missing energy at $\sqrt{s} = 540$ GeV". In: *Phys. Lett. B* 122.1 (1983), p. 103. DOI: 10.1016/0370-2693(83)91177-2.

[2] UA2 Collaboration. "Observation of single isolated electrons of high transverse momentum in events with missing transverse energy at the CERN anti-p p collider". In: *Phys. Lett. B* 122.5-6 (1983), p. 476. DOI: 10.1016/0370-2693(83)91605-2.

[3] UA1 Collaboration. "Experimental observation of lepton pairs of invariant mass around 95 GeV/c^2 at the CERN SPS collider". In: *Phys. Lett. B* 126.5 (1983), p. 398. DOI: 10.1016/0370-2693(83)90188-0.

[4] UA2 Collaboration. "Evidence for $Z^0 \to e^+e^-$ at the CERN anti-p p collider". In: *Phys. Lett. B* 129.1-2 (1983), p. 130. DOI: 10.1016/0370-2693(83)90744-x.

[5] ATLAS Collaboration. In: *Phys. Lett. B* 716 (2012), p. 1. DOI: 10.1016/j.physletb.2012.08.020. arXiv: 1207.7214.

[6] CMS Collaboration. "Observation of a new boson at a mass of 125 GeV with the CMS experiment at the LHC". In: *Phys. Lett. B* 716 (2012), p. 30. DOI: 10.1016/j.physletb.2012.08.021. arXiv: 1207.7235.

[7] Tim Berners-Lee. *Information Management: A Proposal*. https://www.w3.org/History/1989/proposal.html. 1989.

[8] CERN. *CERN, Accelerating Science*. https://cds.cern.ch/record/2280130. 2016.

[9] CERN. *LHC Guide*. https://cds.cern.ch/record/2255762. 2017.

[10] Rende Steerenberg and Anais Schaeffer. *LHC Report: The LHC is full!* https://cds.cern.ch/record/2621245. 2018.

[11] Esma Mobs. *The CERN accelerator complex*. https://cds.cern.ch/record/2197559. 2016.

[12] CMS Collaboration. "The CMS Experiment at the CERN LHC". In: *JINST* 03 (2008), S08004. DOI: 10.1088/1748-0221/3/08/S08004.

[13] CMS Collaboration. *CMS Physics: Technical Design Report Volume 1: Detector Performance and Software*. https://cds.cern.ch/record/922757. 2006.

[14] CMS Collaboration. *CMS technical design report, volume II: Physics performance*. Vol. 34. 6. 2007, p. 995. DOI: 10.1088/0954-3899/34/6/S01.

[15] CMS Collaboration. *Detector Drawings*. https://cds.cern.ch/record/1433717. 2012.

[16] David Barney. *CMS Slice*. https://cds.cern.ch/record/2628641. 2015.

[17] Giles Barr et al. *Particle physics in the LHC era*. First edition. Oxford master series in physics Particle physics, astrophysics, and cosmology; 24. Oxford University Press, 2016.

[18] CMS Collaboration. *CMS Technical Design Report for the Pixel Detector Upgrade*. 2012. DOI: 10.2172/1151650.

[19] CMS Collaboration. "The CMS muon system in Run 2: preparation, status and first results". In: *PoS* EPS-HEP2015 (2015), p. 237. DOI: 10.22323/1.234.0237. arXiv: 1510.05424.

[20] CMS Collaboration. *CMS Technical Design Report for the Level-1 Trigger Upgrade*. https://cds.cern.ch/record/1556311. 2013.

[21] CMS Collaboration. "The CMS trigger in Run 2". In: *PoS* EPS-HEP2017 (2017), p. 523. DOI: 10.22323/1.314.0523.

[22] CMS Collaboration. "The CMS trigger system". In: *JINST* 12.01 (2017), P01020. DOI: 10.1088/1748-0221/12/01/P01020. arXiv: 1609.02366.

[23] Corinne Pralavorio. *Record luminosity: well done LHC*. https://cds.cern.ch/record/2295027. 2017.

[24] CMS Collaboration. *CMS Luminosity - Public Results*. https://twiki.cern.ch/twiki/bin/view/CMSPublic/LumiPublicResults. Accessed: 10/08/2018.

[25] Achintya Rao. *The 2018 data-taking run at the LHC has begun*. https://cds.cern.ch/record/2315786. 2018.

[26] Wikimedia Commons. *File: Standard Model of Elementary Particles*. https://commons.wikimedia.org/w/index.php?title=File:Standard_Model_of_Elementary_Particles.svg&oldid=308836261. Accessed 18-July-2018.

[27] Emmy Noether. "Invariante Variationsprobleme". In: *Nachr. Ges. Wiss. Göttingen, Math.-Phys. Kl.* 1918 (1918), p. 235.

[28] Cottingham W. N. and Greenwood D. A. *An Introduction to the Standard Model of Particle Physics*. Cambridge University Press, 2007.

[29] C. N. Yang and R. L. Mills. "Conservation of Isotopic Spin and Isotopic Gauge Invariance". In: *Phys. Rev.* 96.1 (1954), p. 191. DOI: 10.1103/physrev.96.191.

[30] E598 Collaboration. "Experimental Observation of a Heavy Particle J". In: *Phys. Rev. Lett.* 33.23 (1974), p. 1404. DOI: 10.1103/physrevlett.33.1404.

[31] SLAC-SP-017 Collaboration. "Discovery of a Narrow Resonance in e^+e^- Annihilation". In: *Phys. Rev. Lett.* 33 (1974), p. 1406. DOI: 10.1103/PhysRevLett.33.1406.

[32] S. W. Herb et al. "Observation of a Dimuon Resonance at 9.5 GeV in 400 GeV Proton-Nucleus Collisions". In: *Phys. Rev. Lett.* 39 (1977), p. 252. DOI: 10.1103/PhysRevLett.39.252.

[33] Savely G. Karshenboim. "Precision Study of Positronium: Testing Bound State QED Theory". In: *Int. J. Mod. Phys. A* 19 (2004), p. 3879. DOI: 10.1142/S0217751X04020142. arXiv: hep-ph/0310099.

[34] N. Brambilla et al. "Heavy quarkonium physics". In: *CERN Yellow Report* (2004). arXiv: hep-ph/0412158.

[35] N. Brambilla et al. "Heavy quarkonium: progress, puzzles, and opportunities". In: *Eur. Phys. J. C* 71 (2011), p. 1534. DOI: 10.1140/epjc/s10052-010-1534-9. arXiv: 1010.5827.

[36] BaBar and Belle Collaborations. "The Physics of the B Factories". In: *Eur. Phys. J. C* 74 (2014), p. 3026. DOI: 10.1140/epjc/s10052-014-3026-9. arXiv: 1406.6311.

[37] Geoffrey T. Bodwin, Eric Braaten, and G. Peter Lepage. "Rigorous QCD analysis of inclusive annihilation and production of heavy quarkonium". In: *Phys. Rev. D* 51.3 (1995). Erratum: 10.1103/physrevd.55.5853, p. 1125. DOI: 10.1103/physrevd.51.1125. arXiv: arXiv:hep-ph/9407339.

[38] A. Pineda and J. Soto. "Effective field theory for ultrasoft momenta in NRQCD and NRQED". In: *Nucl. Phys. Proc. Suppl.* 64 (1998), p. 428. DOI: 10.1016/S0920-5632(97)01102-X. arXiv: hep-ph/9707481.

[39] Particle Data Group. "The Review of Particle Physics". In: *Phys. Rev. D* 98.030001 (2018). URL: https://pdg.lbl.gov/.

[40] Ph. Hägler et al. "Towards a solution of the charmonium production controversy: k^- perpendicular factorization versus color octet mechanism". In: *Phys. Rev. Lett.* 86 (2001), pp. 1446–1449. DOI: 10.1103/PhysRevLett.86.1446. arXiv: hep-ph/0004263.

[41] R. Baier and R. Rückl. "Hadronic collisions: A quarkonium factory". In: *Z. Phys. C* 19 (1983), p. 251. DOI: 10.1007/BF01572254.

[42] Harald Fritzsch. "Producing Heavy Quark Flavors in Hadronic Collisions: A Test of Quantum Chromodynamics". In: *Phys. Lett. B* 67 (1977), p. 217. DOI: 10.1016/0370-2693(77)90108-3.

[43] W.E. Caswell and G.P. Lepage. "Effective lagrangians for bound state problems in QED, QCD, and other field theories". In: *Phys. Lett. B* 167.4 (1986), p. 437. DOI: 10.1016/0370-2693(86)91297-9.

[44] G.P. Lepage and B.A. Thacker. "Effective lagrangians for simulating of heavy quark systems". In: *Nucl. Phys. B* 4 (1988), p. 199. DOI: 10.1016/0920-5632(88)90102-8.

[45] Gerhard A. Schuler. "Quarkonium Production: Velocity-Scaling Rules and Long-Distance Matrix Elements". In: *Int. J. Mod. Phys. A* 12.22 (1997), p. 3951. DOI: 10.1142/s0217751x97002103. arXiv: arXiv:hep-ph/9702230.

[46] Pietro Faccioli et al. "Quarkonium production at the LHC: A data-driven analysis of remarkably simple experimental patterns". In: *Phys. Lett. B* 773 (2017), p. 476. DOI: 10.1016/j.physletb.2017.09.006. arXiv: 1702.04208.

[47] Mathias Butenschoen and Bernd A. Kniehl. "J/ψ Polarization at the Tevatron and the LHC: Nonrelativistic-QCD Factorization at the Crossroads". In: *Phys. Rev. Lett.* 108 (2012), p. 172002. DOI: 10.1103/PhysRevLett.108.172002. arXiv: 1201.1872.

[48] Pietro Faccioli et al. "Towards the experimental clarification of quarkonium polarization". In: *Eur. Phys. J. C* 69 (2010), pp. 657–673. DOI: 10.1140/epjc/s10052-010-1420-5. arXiv: 1006.2738.

[49] Pietro Faccioli et al. "Determination of χ_c and χ_b polarizations from dilepton angular distributions in radiative decays". In: *Phys. Rev. D* D83 (2011), p. 096001. DOI: 10.1103/PhysRevD.83.096001. arXiv: 1103.4882.

[50] ATLAS Collaboration. "Observation of a new χ_b state in radiative transitions to $\Upsilon(1S)$ and $\Upsilon(2S)$ at ATLAS". In: *Phys. Rev. Lett.* 108 (2012), p. 152001. DOI: 10.1103/PhysRevLett.108.152001. arXiv: 1112.5154.

[51] D0 Collaboration. "Observation of a narrow mass state decaying into $\Upsilon(1S) + \gamma$ in anti-p p collisions at $\sqrt{s} = 1.96$ TeV". In: *Phys. Rev. D* 86 (3 2012), p. 031103. DOI: 10.1103/PhysRevD.86.031103. arXiv: 1203.6034.

[52] CMS Collaboration. "Observation of the $\chi_{b1}(3P)$ and $\chi_{b2}(3P)$ and measurement of their masses". In: *Phys. Rev. Lett.* (2018). Submitted to Phys. Rev. Lett. DOI: 10.3204/PUBDB-2018-02193. arXiv: 1805.11192.

[53] LHCb Collaboration. "Study of χ_b meson production in pp collisions at $\sqrt{s} = 7$ and 8 TeV and observation of the decay $\chi_b(3P) \to \Upsilon(3S)\gamma$". In: *Eur. Phys. J. C* 74.10 (2014), p. 3092. DOI: 10.1140/epjc/s10052-014-3092-z. arXiv: 1407.7734.

[54] CDF Collaboration. "Production of $\Upsilon(1S)$ mesons from χ_b decays in anti-p p collisions at $\sqrt{s} = 1.8$ TeV". In: *Phys. Rev. Lett.* 84 (2000), p. 2094. DOI: 10.1103/PhysRevLett.84.2094. arXiv: hep-ex/9910025.

[55] LHCb Collaboration. "Measurement of the Υ polarizations in pp collisions at $\sqrt{s} = 7$ and 8 TeV". In: *JHEP* 12 (2017), p. 110. DOI: 10.1007/JHEP12(2017)110. arXiv: 1709.01301.

[56] CMS Collaboration. "Measurement of the $\Upsilon(1S), \Upsilon(2S)$ and $\Upsilon(3S)$ polarizations in pp collisions at $\sqrt{s} = 7$ TeV". In: *Phys. Rev. Lett.* 110.8 (2013), p. 081802. DOI: 10.1103/PhysRevLett.110.081802. arXiv: 1209.2922.

[57] CDF Collaboration. "Measurements of Angular Distributions of Muons From Υ Meson Decays in $p\bar{p}$ Collisions at $\sqrt{s} = 1.96$ TeV". In: *Phys. Rev. Lett.* 108 (2012), p. 151802. DOI: 10.1103/PhysRevLett.108.151802. arXiv: 1112.1591.

[58] CMS Collaboration. "Performance of Photon Reconstruction and Identification with the CMS Detector in Proton-Proton Collisions at $\sqrt{(s)}$ = 8 TeV". In: *JINST* 10.08 (2015), P08010. DOI: 10.1088/1748-0221/10/08/P08010. arXiv: 1502.02702.

[59] Kirill Prokofiev and Thomas Speer. *A kinematic and a decay chain reconstruction library*. http://cds.cern.ch/record/865614. 2005.

[60] Pietro Faccioli et al. "From identical S- and P-wave p_T spectra to maximally distinct polarizations: probing NRQCD with χ states". In: *Eur. Phys. J. C* 78.3 (2018), p. 268. DOI: 10.1140/epjc/s10052-018-5755-7. arXiv: 1802.01106.

[61] Muriel Pivk and Francois R. Le Diberder. "sPlot: A statistical tool to unfold data distributions". In: *Nucl. Instrum. Meth. A* 555 (2005), p. 356. DOI: 10.1016/j.nima.2005.08.106. arXiv: physics/0402083.

[62] Souvik Das. "A simple alternative to the Crystal Ball function". In: (2016). arXiv: 1603.08591.

[63] Pietro Faccioli et al. “Quarkonium production in the LHC era: A polarized perspective”. In: *Physics Letters B* 736 (2014), p. 98. DOI: 10.1016/j.physletb.2014.07.006. arXiv: 1403.3970.

List of Abbreviations

ALICE A Large Ion Collider Experiment.

ATLAS A Toroidal LHC Apparatus.

CB Crystal Ball.

CDF Collider Detector at Fermilab.

CEM color evaporation model.

CERN European Organization for Nuclear Research.

CMS Compact Muon Solenoid.

CS Collins-Soper.

CSC Cathode Strip Chamber.

CSM color singlet model.

DSCB double-sided CB.

DT Drift Tube.

ECAL Electromagnetic Calorimeter.

EFT effective field theory.

GT Global Trigger.

HCAL Hadron Calorimeter.

HEPHY Institut für Hochenergiephysik.

HLT High Level Trigger.

HX helicity.

IP interaction point.

KVF kinematic vertex fit.

L1 Level-1.

L1T Level-1 trigger.

LDME long-distance matrix element.

LHC Large Hadron Collider.

LHCb LHC beauty.

Linac2 linear accelerator 2.

LO leading order.

MC Monte Carlo.

NLO next-to-leading order.

NRQCD nonrelativistic QCD.

PDF probability density function.

PDG Particle Data Group.

PES photon-energy scale.

pNRQCD potential NRQCD.

pp proton-proton.

PS Proton Synchrotron.

PSB Proton Synchrotron Booster.

PX perpendicular-helicity.

QCD quantum chromodynamics.

QED quantum electrodynamics.

RPC Resistive Plate Chamber.

SDC short-distance coefficient.

SM standard model.

SPS Super Proton Synchrotron.

SUSY supersymmetry.

WWW World Wide Web.

ÖAW Österreichische Akademie der Wissenschaften.

List of Figures

List of Tables